Environmental and Storm-Scale Controls on Close Proximity Supercells Observed by TORUS on 8 June 2019

MATTHEW B. WILSON,[a] ADAM L. HOUSTON,[a] CONRAD L. ZIEGLER,[b,c] DANIEL M. STECHMAN,[d,b] BRIAN ARGROW,[e] ERIC W. FREW,[e] SARA SWENSON,[e] ERIK RASMUSSEN,[d,b] AND MICHAEL CONIGLIO[b,c]

[a] *University of Nebraska–Lincoln, Lincoln, Nebraska*
[b] *National Oceanic and Atmospheric Administration/National Severe Storms Laboratory, Norman, Oklahoma*
[c] *School of Meteorology, University of Oklahoma, Norman, Oklahoma*
[d] *Cooperative Institute for Severe and High-Impact Weather Research and Operations, Norman, Oklahoma*
[e] *Ann and H. J. Smead Department of Aerospace Engineering Sciences, University of Colorado Boulder, Boulder, Colorado*

(Manuscript received 6 January 2023, in final form 30 August 2023, accepted 5 September 2023)

ABSTRACT: The Targeted Observation by Radars and UAS of Supercells (TORUS) field project observed two supercells on 8 June 2019 in northwestern Kansas and far eastern Colorado. Although these storms occurred in close spatial and temporal proximity, their evolutions were markedly different. The first storm struggled to maintain itself and eventually dissipated. Meanwhile, the second supercell developed just after and slightly to the south of where the first storm dissipated, and then tracked over almost the same location before rapidly intensifying and going on to produce several tornadoes. The objective of this study is to determine why the first storm struggled to survive and failed to produce mesocyclonic tornadoes while the second storm thrived and was cyclically tornadic. Analysis relies on observations collected by the TORUS project—including unoccupied aircraft system (UAS) transects and profiles, mobile soundings, surface mobile mesonet transects, and dual-Doppler wind syntheses from the NOAA P-3 tail Doppler radars. Our results indicate that rapid changes in the low-level wind profile, the second supercell's interaction with two mesoscale boundaries, an interaction with a rapidly intensifying new updraft just to its west, and the influence of a strong outflow surge likely account for much of the second supercell's increased strength and tornado production. The rapid evolution of the low-level wind profile may have been most important in raising the probability of the second supercell becoming tornadic, with the new updraft and the outflow surge leading to a favorable storm-scale evolution that increased this probability further.

KEYWORDS: Severe storms; Tornadoes; Unpiloted aerial systems; Mesoscale forecasting

1. Introduction

The near-storm environment greatly influences the organization, intensity, and longevity of deep convection, with more intense, organized storm modes such as bow echoes and supercells expected with greater values of environmental shear and instability (e.g., Rasmussen and Blanchard 1998; Thompson et al. 2003; Craven and Brooks 2004; Smith et al. 2012). Even within a given storm mode, hazard production can be strongly modulated by environmental conditions. For example, supercells are more likely to produce tornadoes in environments with stronger low-level shear, higher values of low-level storm-relative helicity, and lower lifted condensation level (LCL) heights (e.g., Thompson et al. 2003; Coffer et al. 2019). However, hazard production can vary wildly between supercells in close spatial and temporal proximity in ostensibly similar synoptic- or meso-alpha-scale environments (Klees et al. 2016; Bunkers et al. 2022; Healey and Van Den Broeke 2023). This likely indicates that other factors besides the characteristics of the larger-scale inflow environment likely exert strong influences on the strength and behavior of individual supercells. These factors include the presence of mesoscale heterogeneities in the near-storm environment (e.g., Maddox et al. 1980; Markowski et al. 1998; Atkins et al. 1999; Rasmussen et al. 2000), rapid changes in the near-storm environment over time (e.g., Koch et al. 2016; Klees et al. 2016; King et al. 2017; Gropp and Davenport 2018), interactions or mergers between storms (e.g., Lee et al. 2006; Bluestein and Weisman 2000; Rogers and Weiss 2008; Hastings and Richardson 2016; Klees et al. 2016), differences in the initial forcing for deep convection initiation (e.g., Brooks and Wilhelmson 1992; Naylor and Gilmore 2012; Flournoy and Rasmussen 2023), and internal processes within a supercell (e.g., Coffer and Parker 2017; Markowski 2020; Flournoy et al. 2020).

Of these factors, the one which has been most intensely studied in recent years is likely the influence of environmental heterogeneities (and especially mesoscale boundaries) on supercell evolution. Previous modeling and observational studies have often found that supercell–boundary interactions can lead to storm intensification and promote tornadogenesis (e.g., Maddox et al. 1980; Markowski et al. 1998; Atkins et al. 1999; Rasmussen et al. 2000; Laflin and Houston 2012; Magee and Davenport 2020). Supercells which interact with boundaries may become more intense due to the ingestion of boundary-generated baroclinic streamwise vorticity (Atkins et al. 1999; Rasmussen et al. 2000), from the presence of low-level convergence along the boundary enhancing the storm's low-level updraft (Laflin and

Supplemental information related to this paper is available at the Journals Online website: https://doi.org/10.1175/MWR-D-23-0002.s1.

Corresponding author: Matthew B. Wilson, mwilson41@huskers.unl.edu

DOI: 10.1175/MWR-D-23-0002.1

Houston 2012; Honda and Kawano 2016), from the stretching of near-surface vertical vorticity along the boundary into the storm's low-level mesocyclone (Maddox et al. 1980; Wakimoto et al. 1998), or from the presence of high θ_E air and enhanced low-level instability along and just on the cool side of the boundary (Maddox et al. 1980; Rasmussen et al. 2000). However, supercell–boundary interactions can lead to storm weakening or dissipation if convective inhibition (CIN) on the cool side of the boundary is too great (Ziegler et al. 2010; Davenport and Parker 2015). Moreover, the angle of a supercell's interaction with a boundary may also be important, with storms moving parallel to the boundary maximizing their residence time in the zone of enhanced streamwise vorticity along the boundary and storms moving perpendicular to the boundary quickly moving into less-favorable conditions deeper in the cool air mass and minimizing their chances for intensification (Markowski et al. 1998; Atkins et al. 1999; Magee and Davenport 2020).

Rapid changes in a storm's environment over time can also impact its evolution. These changes can potentially lead to differences between storms in close spatial and temporal proximity. Examples of such changes can include rapid low-level destabilization (Koch et al. 2016; King et al. 2017), sharp increases in low-level wind shear and SRH (Koch et al. 2016), and the increasing CIN and stronger low-level kinematics associated with the early evening transition period (EET; Maddox 1993; Mead and Thompson 2011; Gropp and Davenport 2018; Brown et al. 2021; Davenport 2021). For example, the tornadic supercell examined by Klees et al. (2016) experienced an increase in low-level SRH in the evening which was not experienced by its nontornadic counterpart, since that storm's inflow and organization were disrupted by a cell merger beforehand. Such increases in low-level shear and SRH as the boundary layer decouples during the EET have been found to be particularly favorable for tornado formation, with Mead and Thompson (2011) noting 100–200 $m^2 s^{-2}$ increases in effective SRH from 0000 to 0300 UTC in a sample of nocturnal significant tornado cases in the Great Plains and Davenport (2021) noting that increases in low-level shear and SRH often preceded tornado reports in long-lived supercells. Simulations of supercells encountering increases in low-level shear and SRH during the EET have shown that the strengthening low-level shear provides more streamwise vorticity for the supercell updraft to tilt (Coffer and Parker 2015). This strengthens the mid- and low-level mesocyclones, lowers the base of the low-level mesocyclone, and strengthens the low-level updraft through stronger vertical perturbation pressure gradient accelerations from the stronger, lower-based mesocyclone above (Markowski et al. 2012; Markowski and Richardson 2014; Coffer and Parker 2015).

Storm mode, longevity, and intensity can also be affected by interactions and mergers with other storms. Storm mergers can be constructive, leading to the intensification of the dominant storm, the development or strengthening of a low-level mesocyclone, and possibly tornadogenesis (Lee et al. 2006; Wurman et al. 2007; Rogers and Weiss 2008; Rogers 2012; Hastings and Richardson 2016), or destructive, leading to the weakening, dissipation, or upscale growth of the dominant storm (Bluestein and Weisman 2000; Hastings and Richardson 2016; Klees et al. 2016). Constructive interactions may be more likely to occur when an ancillary cell merges into the rear flank of a supercell (Rogers and Weiss 2008; Hastings and Richardson 2016; Fischer and Dahl 2022), while mergers into a supercell's forward flank or mesocyclone may be more likely to be disruptive (Rogers and Weiss 2008; Hastings and Richardson 2016). Emphasizing the range of possible outcomes of a given storm merger depending on the relative positions and strengths of the merging cells, Flournoy et al. (2022) found a wide range of postmerger changes in low-level rotation strength in a large sample of observed supercells undergoing cell mergers, with mergers of longer duration and involving more cells more likely to result in mesocyclone strengthening. Furthermore, mesocyclones that were weak at the beginning of a cell merger were more likely to strengthen after the merger, while stronger mesocyclones tended to weaken after mergers (Flournoy et al. 2022).

Supercell evolution may also be impacted by the size and strength of the initial area of forcing for convection initiation (CI). For example, since broader supercell updrafts are less prone to entrainment (Peters et al. 2020), a broader area of initial deep convection may be able to organize into a stronger supercell than a smaller area of initial deep convection in the same environment. Little is known about how this affects the evolution of observed supercells, but the limited number of numerical modeling studies that have examined the sensitivity of simulated supercells to the mechanism used to initiate them have found that variations in the size, intensity, and location of the initiating warm bubble or area of updraft nudging in the model can have an effect on the evolution of the simulated storm (Brooks and Wilhelmson 1992; Naylor and Gilmore 2012; Flournoy and Rasmussen 2023). In particular, simulations conducted by Flournoy and Rasmussen (2023) showed that modeled supercells emerging from a stronger area of forcing for CI developed strong updrafts more quickly, had storm motions more deviant from the mean flow, and developed strong near-surface rotation sooner.

Storms which initiate in nearly identical environments and in almost the same manner can still evolve differently through the consequences of processes occurring within the storm itself or through its interaction with boundary layer turbulence. Several modeling studies (Coffer et al. 2017; Markowski 2020; Flournoy et al. 2020) have initiated ensembles of supercells in identical or nearly identical environmental conditions using techniques to add a small amount of ensemble spread in initial conditions well below that which would be observable by available observing platforms. In experiments using environments extremely favorable for tornadoes, all members produced tornadoes (Markowski 2020). However, in environments less favorable for tornado formation, the ensembles often included tornadic and nontornadic storms (Coffer et al. 2017; Flournoy et al. 2020). Within a given ensemble, these studies found few storm-scale differences which consistently separated tornadic storms from nontornadic ones or significantly tornadic storms from those producing only weak tornadoes. However, some storm-scale differences were apparent between storms initialized in highly favorable environments and those in less-favorable environments for tornadogenesis. In highly favorable environments, low-level updrafts were stronger and steadier, cold outflow was

located farther from the low-level mesocyclone, and a more coherent boundary was noted emanating from the forward flank toward the low-level mesocyclone (Coffer and Parker 2017; Flournoy et al. 2020). Moreover, recent observational work has found some differences in the structure and behavior of tornadic and nontornadic supercells in close proximity, including greater deviant rightward motion in tornadic supercells as compared to their nontornadic neighbors (Coniglio and Parker 2020; Bunkers et al. 2022) and larger updrafts (as inferred from larger Z_{DR} column areas) in tornadic supercells (Healey and Van Den Broeke 2023).

While most of the studies listed above attempt to isolate the influence of one particular mesoscale process on a supercell, it is important to note that a given storm may be influenced by several of these processes, sometimes simultaneously. When multiple processes are present, they may combine constructively or destructively. An example of a constructive combination of these processes would be if a supercell underwent a storm merger which strengthened it at the same time as low-level shear rapidly increased during the EET. Conversely, the nontornadic supercell in the tornadic–nontornadic supercell pair examined by Klees et al. (2016) is an excellent example of how these processes can combine destructively, as it underwent a destructive storm merger which caused it to dissipate before it could encounter the increase in low-level shear observed during the EET. One way to examine how these processes can act in various combinations to cause proximate storms to be different is through detailed case studies of observed pairs of proximate tornadic and nontornadic supercells. To the authors' best knowledge, the proximate tornadic–nontornadic supercell pair examined by Klees et al. (2016) is the only prior example of such a case study. Thus, more work is needed to examine how these processes interact in particular events and which processes are most important in influencing the evolution of a given storm when multiple mesoscale processes are present. This paper presents another such case study from a dataset collected on a proximate tornadic–nontornadic supercell pair during the Targeted Observation by Radars and UAS of Supercells (TORUS; Houston et al. 2020) field project.

On 8 June 2019, TORUS observed two supercells in close spatial and temporal proximity that behaved very differently. The first supercell initiated just west of Burlington, Colorado, around 1930 UTC, produced a brief landspout tornado soon after initiating, and then tracked west into northwest Kansas before dissipating around 2200 UTC. The second supercell developed out of an area of convection which initiated just after 2230 UTC and then consolidated into a supercell around 2300 UTC less than 15 miles south of where the first storm dissipated in northwest Kansas. This storm went on to rapidly intensify, turn right, and produce several mesocyclonic tornadoes before merging into a bow echo around 0400 UTC 9 June. TORUS collected detailed observations of both storms and their environments using mobile and airborne radars, mobile mesonets, targeted radiosonde launches, unoccupied aircraft systems (UASs), and a lidar. In this article, we use these special observations collected by TORUS, along with more conventional, operationally available datasets, to investigate the following questions about the evolution of these two supercells:

1) Why was the second supercell able to initiate and thrive in almost the same location where the first supercell struggled and dissipated less than an hour before?
2) What accounts for the drastic differences in the structure and hazard production of these two supercells in such close spatial and temporal proximity?

Section 2 will give a short overview of TORUS operations during the 8 June 2019 intensive observing period (IOP), the datasets used to examine each supercell and their changing environments, and the analysis techniques used for each. Section 3 will describe the evolution of each storm and use these datasets to examine possible reasons for their very different characteristics, with a focus on the factors outlined in the introduction which may cause two supercells in close proximity to evolve differently. Finally, section 4 will summarize the results of our analysis and will discuss possible avenues for future research.

2. Data and methods

a. TORUS datasets and analysis techniques

1) MOBILE RADIOSONDES

To examine the near-storm and far-field environment, the TORUS team launched multiple radiosondes each day. These launches collected deep tropospheric profiles of temperature, pressure, relative humidity, wind speed, and wind direction using Vaisala RS41-SGP radiosondes (Waugh 2020a). In this paper, the SharpPy and MetPy Python packages (Blumberg et al. 2017; May et al. 2022) are used to visualize these profiles and calculate various thermodynamic and kinematic parameters from them, with all thermodynamic parameters calculated using SharpPy for consistency. Far-field soundings on 8 June 2019 were released between 35 and 65 km away from the target supercells.

2) MOBILE MESONETS

TORUS collected high-resolution near-surface observations of pressure, temperature, relative humidity, wind speed, and wind direction using mobile mesonet vehicles operated by the University of Oklahoma (Waugh 2020b), as well as Combined Mesonet and Tracker (CoMeT) vehicles operated by the University of Nebraska (Houston et al. 2021). The mobile mesonet and CoMeT vehicles both used an aspirated U-tube (Waugh 2021) shield to protect their temperature and relative humidity sensors from solar radiation and precipitation. Wind speed and direction on both platforms were measured using RM Young 05103 anemometers.

3) P-3 DATA AND DUAL-DOPPLER ANALYSES

To conduct a detailed examination of the internal structure and evolution of each of the 8 June 2019 supercells, dual-Doppler analyses were created from data collected by the NOAA P-3 tail Doppler radars (TDRs; Ziegler 2020) during the 8 June IOP. The P-3 TDRs operate at X-band and are situated on the aircraft such that one collects a conical scan with the axis of the cone facing backward along the aircraft's direction of travel and the other

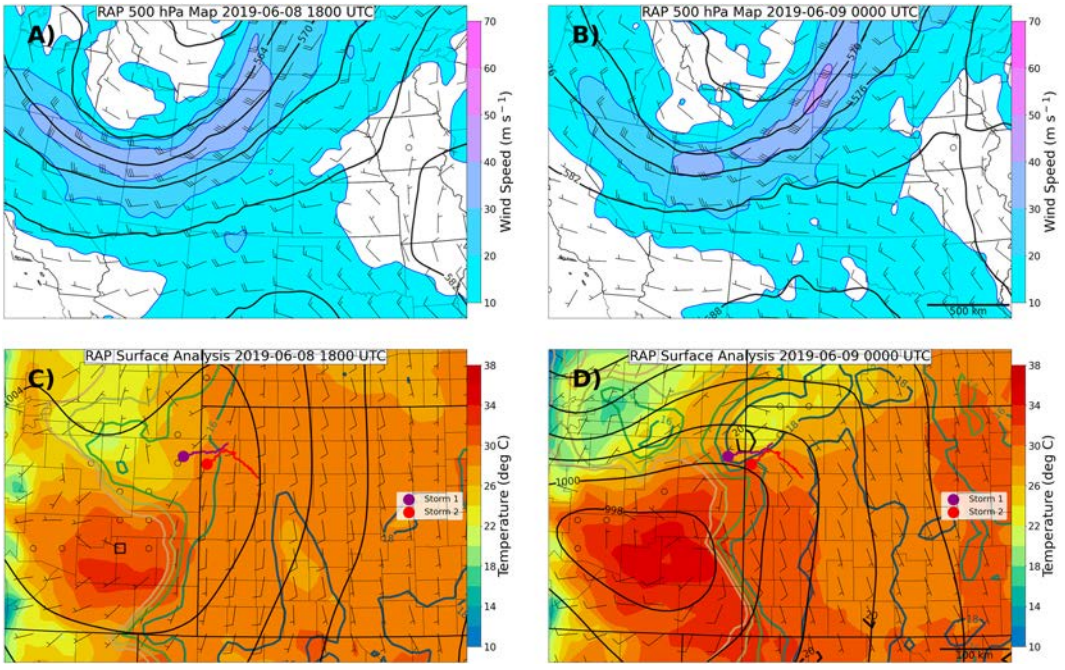

FIG. 1. (a),(b) Plots of 500-hPa height (dam) and wind (m s^{-1}) and (c),(d) surface temperature (shaded; °C), dewpoint (green contours every 2°C from 10° to 20°C), mean sea level pressure (contoured every 4 hPa in black), and 10-m winds (plotted as barbs; m s^{-1}) data from 13-km resolution RAP (Benjamin et al. 2016) analyses from 1800 UTC 8 Jun 2019 and 0000 UTC 9 Jun 2019. Surface analyses in (c) and (d) are focused more closely on west Kansas and east Colorado to show detail. The formation location of storm 1 (storm 2) is plotted in (c) and (d) as a purple (red) dot, and the track of the reflectivity centroid of storm 1 (storm 2) is plotted as a purple (red) line. RAP data were obtained from the THREDDS server maintained by NCEI at https://www.ncei.noaa.gov/thredds/catalog/model-rap130anl-old/catalog.html.

conducts a conical scan with the axis of the cone facing forward along the aircraft's direction of travel. This setup is ideal for dual-Doppler analyses, since the beams from the two radars cross at an angle suitable for retrieving the three-dimensional wind as the aircraft flies past a storm. For more details on the configuration of the TDRs, see Jorgensen et al. (2017) and Ziegler et al. (2018).

To create the dual-Doppler velocity syntheses used in this paper, the P-3 TDR data were first run through a multistep quality control process. The NCAR Solo3 software (https://www.eol.ucar.edu/software/solo3) was used to remove the aircraft velocity from the TDR data. A custom Python editing script developed initially by the Biggerstaff group at the University of Oklahoma (Alford et al. 2022) that was subsequently enhanced by D. Stechman (CIWRO/NSSL) and the third coauthor (CLZ) with several additional editing functions for both airborne and ground-based radars was then applied to perform a bulk initial quality control of the entire TDR dataset. This enhanced script used the Python ARM Radar Toolkit (PyART; Helmus and Collis 2016) to remove main- and sidelobe ground echoes and velocities, correct dual-PRF processing errors in the velocity measurements, remove (despoke) biased radials, and remove noisy velocities. Although the script could also be employed to perform PyART dealiasing, more reliable results were obtained by instead examining script-edited sweeps in Solo3 and manually dealiasing any folded velocities.

The quality-controlled data from each TDR were next split into volumes, with each volume corresponding to a single pass of the P-3 by the storm. Due to developing convection along the flanking line and in the inflow of storm 2, as well as the storm's large size, these volumes were collected at a slightly larger setback distance than would normally be used by the P-3 during TORUS data collection and also represented a slightly longer period of time (6–8 min each) than would usually be the case for P-3 deployments during TORUS. Data from each radar in each volume were objectively analyzed to a common storm-centered three-dimensional Cartesian grid with 250-m grid spacing in all coordinate directions and 77 vertical levels from the surface to 19 km (with the lowest vertical level at 0 km AGL) and horizontal dimensions of 87.5 km × 87.5 km. The single-radar objective analyses employed a single-pass Barnes spatial interpolation scheme with a smoothing parameter value of $k = 0.5369$ (Barnes 1964; Koch et al. 1983; Majcen et al. 2008; Ziegler 2013). All data were gridded following time-to-space position adjustment with storm motion to a nominal analysis time (e.g., Ziegler 2013) that approximated the average time of the fore and aft TDR sweeps through the storm core region, thus minimizing any advection corrections of the 3-s interval TDR sweeps in the evolving main updraft and mesocyclone.

Following dual-TDR objective analyses of given volumes, a series of dual-Doppler airflow syntheses were performed to

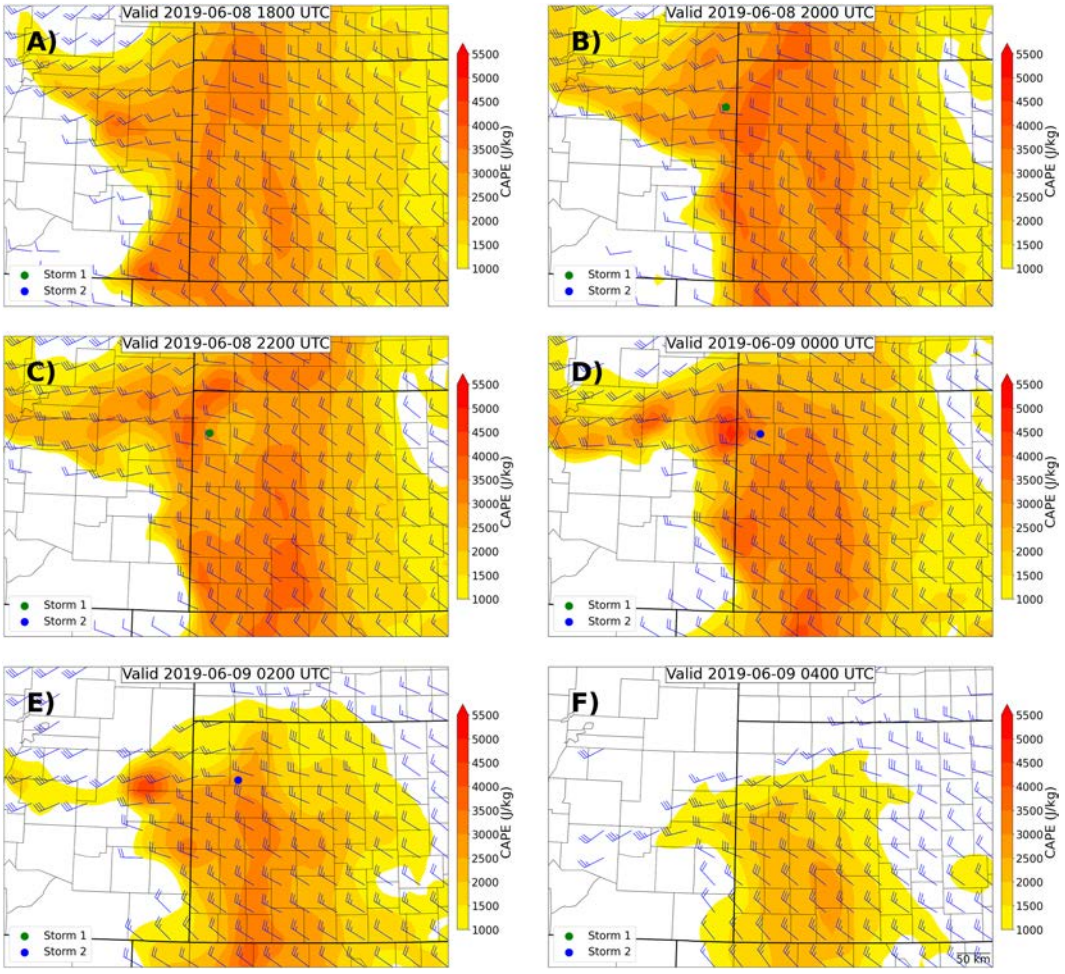

FIG. 2. RAP analyses of CAPE (shaded; J kg^{-1}) and surface–6-km bulk wind difference (barbs; m s^{-1}) for 1800 UTC 8 Jun 2019–0400 UTC 9 Jun 2019 over west Kansas and east Colorado. When present, the reflectivity centroid of storm 1 (storm 2) is marked with a green (blue) dot.

retrieve the three-dimensional wind and reflectivity fields (Ray et al. 1980; Ray and Sangren 1983; Kessinger et al. 1987; Ziegler 2013). The anelastic mass continuity equation was iteratively integrated from the top of the volume downward in each grid column with two linear equations relating the vector wind components to the TDR velocities and a reflectivity-based particle fall speed, yielding an initial estimate of the three-dimensional wind field (Kessinger et al. 1987; Ziegler 2013). Missing horizontal vector winds in areas of the domain outside of the storm without reliable dual-TDR radial velocity measurements were then replaced with data from the 2357 UTC far-field sounding (gridded to match the 250-m vertical spacing of the objective analyses) with imposition of the fixed radar-analyzed winds as lateral boundary conditions via 2D low-pass filtering (Ziegler 2013). After integrating mass continuity to extend vertical velocities through the latter hole-filled horizontal divergence sublayers (e.g., Nelson and Brown 1982), an O'Brien scheme (O'Brien 1970) set a kinematic lower boundary condition of $w = 0$ m s^{-1} at the surface to adjust the vertical velocities in each grid column. The resulting vertical velocity field was then horizontally smoothed using a 2D Raymond sixth-order filter (Raymond 1988). Finally, a 3D-variational technique imposing anelastic mass continuity as an exact local constraint was used to retrieve the final three-dimensional wind field (Ray et al. 1978).

4) UAS

During TORUS, the RAAVEN UAS was used to collect data above the surface within the PBL in storm outflow and in the near-storm environment. The RAAVEN configuration used during TORUS measures pressure, temperature, and relative humidity and uses a multihole probe (MHP) built by Black Swift Technologies to measure wind speed and direction (Frew et al. 2020). In addition, the MHP contains an iMET EE03 radiosonde to collect additional pressure, temperature, and relative humidity measurements. For a more detailed description of the RAAVEN airframe, sensor characteristics, and

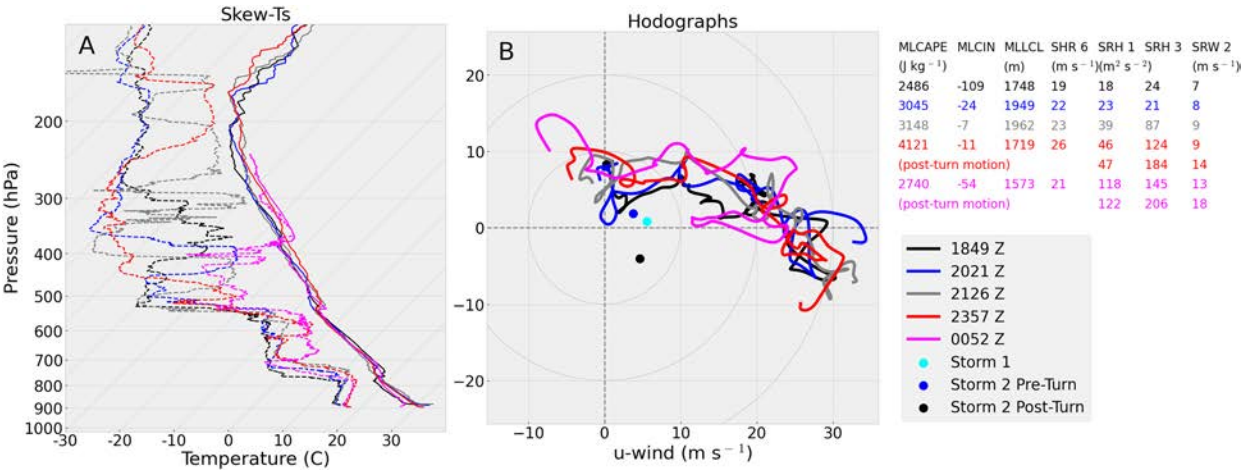

FIG. 3. (a) Skew T plots and (b) hodographs for all 8 Jun 2019 far-field soundings from TORUS from 1800 to 0100 UTC 9 Jun. A table of selected parameters from each sounding is included to the right of (b). All SRH and SR flow parameters are calculated with observed storm motions. For storm 1, an observed motion of 5.6 m s^{-1} from 262° was used, while a motion of 4.4 m s^{-1} from 244° was used for the motion of storm 2 before its sharp right turn and a motion of 6.1 m s^{-1} from 311° was used after the turn. The sharp right turn of storm 2 took place between 0045 and 0100 UTC. For legibility, a Gaussian filter with $\sigma = 20$ is used to smooth the winds from each sounding plotted on the hodograph.

sensor locations, see Frew et al. (2020). The siting of the MHP on the aircraft made it vulnerable to wet bulbing from exposure to precipitation and to solar heating. Data used in this study were thus carefully checked for evidence of wet bulbing. Since data collected by the UAS on 8 June were all collected under cloud cover, the impact of solar heating of the sensors should be minimal. For the analyses presented here, the MHP data were thinned to a temporal spacing of 1 Hz and a first-order time response correction was applied to account for the 11-s time constant of the MHP-UAS assembly.

b. *Case overview and TORUS operations overview*

The synoptic setup on 8 June 2019 was broadly favorable for severe weather over the high Plains of eastern Colorado, northwestern Kansas, and western Nebraska. Aloft, a broad trough occupied much of the intermountain west and was beginning to emerge onto the Plains during the afternoon and evening of the 8th (Fig. 1). At the surface, a lee cyclone had developed on the Plains of eastern Colorado during the day, a cold front extended from the Dakotas to western Nebraska before curving westward across northeastern Colorado, and a dryline extended from the cold front in eastern Colorado southward across the western high Plains (Fig. 1). Over the course of the day, the surface cyclone and cold front both drifted southward, while the dryline mixed eastward during the afternoon before retreating westward during the evening. A parameter space favorable for supercells existed near the cold front–dryline intersection in eastern Colorado and northwestern Kansas, with surface–6-km bulk wind differences of 30–40 kt (1 kt ≈ 0.51 m s^{-1}) and 2000–4000 J kg^{-1} of MLCAPE shown on both RAP analyses (Fig. 2) and a sounding launched by TORUS at 1849 UTC in Sharon Springs, Kansas, just before deep convection initiation (Fig. 3a).

In this environment, initial convection near the triple point developed into a marginal supercell by 2000 UTC (Figs. 4a, 5, and 6a,c). TORUS sampled this storm (hereafter "storm 1") from 2000 UTC to just after 2200 UTC, although the surface mobile mesonets, UASs, and ground-based radars were only present for part of this period. During this time, storm 1 remained fairly weak, with 7 km AGL vertical velocities never exceeding 30 m s^{-1} in the available P-3 dual-Doppler analyses (Figs. 5b and 6a). It also never displayed an organized low-level (1 km AGL) updraft or mesocyclone (Figs. 5b,c and 6c). Storm 1 began to dissipate around 2200 UTC (Figs. 4b,c and 5b), at which time the TORUS armada stopped sampling the storm. Although no mesocyclonic tornadoes were observed from this storm, a landspout tornado was noted with this cell from 1958 to 2001 UTC (NCEI Storm Events Database, https://www.ncdc.noaa.gov/stormevents/).

Around 2230 UTC, a new cluster of convection developed near the triple point, and the southern end of this cluster rapidly consolidated into a new supercell just after 2300 UTC (Fig. 4d, a more detailed animation of Goodland, Kansas (KGLD), reflectivity from 1930 to 0300 UTC is included in the online supplemental material). TORUS redeployed to this storm (hereafter "storm 2"), with the P-3 beginning its sampling by 2313 UTC and the ground teams arriving around 2345 UTC. Prior to the arrival of the TORUS team, storm 2 began to interact with two mesoscale boundaries (the possible effects of which are discussed in section 3). Storm 2 already had a stronger midlevel updraft than storm 1 on the first P-3 dual-Doppler analysis at 2313 UTC (Fig. 5b) Storm 2 turned sharply rightward and intensified further after 0000 UTC 9 June (Figs. 4e,f and 5), developing a tight, well-defined low-level mesocyclone by 0105 UTC (Figs. 5c and 6d). As it intensified, storm 2 underwent an interaction with a new updraft which developed over its rear-flank outflow, explosively intensified, and took over as the primary updraft of storm 2 (Fig. 5). Simultaneously, a strong outflow surge swept around the rear of storm 2 (Fig. 5c) and low-level shear and SRH sharply increased

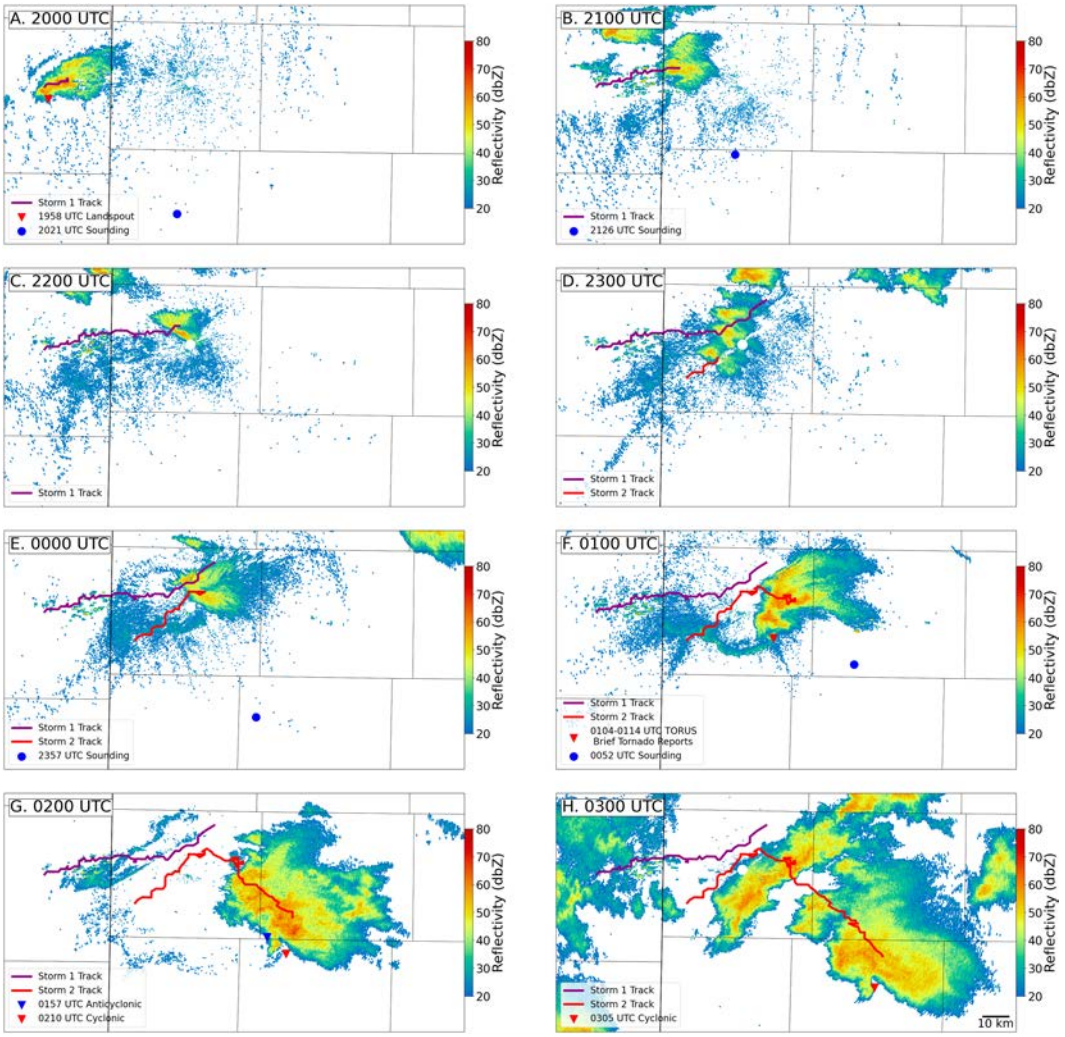

FIG. 4. Overview of the life cycle of both 8 Jun 2019 supercells, showing reflectivity from KGLD at (a) 2000, (b) 2100, (c) 2200, (d) 2300, (e) 0000, (f) 0100, (g) 0200, and (h) 0300 UTC. Manually analyzed tracks of both storms are plotted in each image from their respective initiation times until the time of the image, and sounding launch locations (blue dots) and tornado reports (red triangles) are plotted on the image closest in time to the sounding launch or tornado start time.

during the EET. The effects of these processes on storm 2 are discussed in detail in section 3. At its peak intensity at 0105 UTC, storm 2 had an updraft exceeding 60 m s^{-1} at 7 km AGL, with updraft velocities exceeding 10 m s^{-1} covering almost 250 km^2 (Figs. 5a,b and 6b). Between 0104 and 0114 UTC, the TORUS team reported several gustnadoes or possible weak tornadoes (Table 1); however, the first tornado report in the NCEI Storm Events Database from this cell is a brief anticyclonic tornado at 0157 UTC. Storm 2 would go on to produce cyclonic tornadoes from 0210 to 0226 UTC and from 0305 to 0307 UTC (Figs. 4g,h) before merging with a larger convective complex around 0400 UTC. These last two tornadoes occurred well after coordinated data collection ended at 0112 UTC with the final UAS landing, although some individual teams continued observations beyond this point.

3. Results and discussion

a. Environmental evolution

As discussed previously in the synoptic overview, the pre-CI environment on 8 June 2019 was characterized by sufficient shear and instability for supercells. Convection initiated in this environment around 1930 UTC and quickly became a supercell, the inflow environment of which was sampled by the TORUS far-field sounding team at 2021 and 2127 UTC. These later soundings showed that the environment in northwest Kansas continued to appear suitable for supercells, with over 40 kt (21 m s^{-1}) of deep-layer shear and 3000 J kg^{-1} of CAPE and minimal CIN (Fig. 3). However, LCL heights on both soundings were fairly high (Fig. 7d). Furthermore, the low-level hodograph on both soundings displayed weak flow

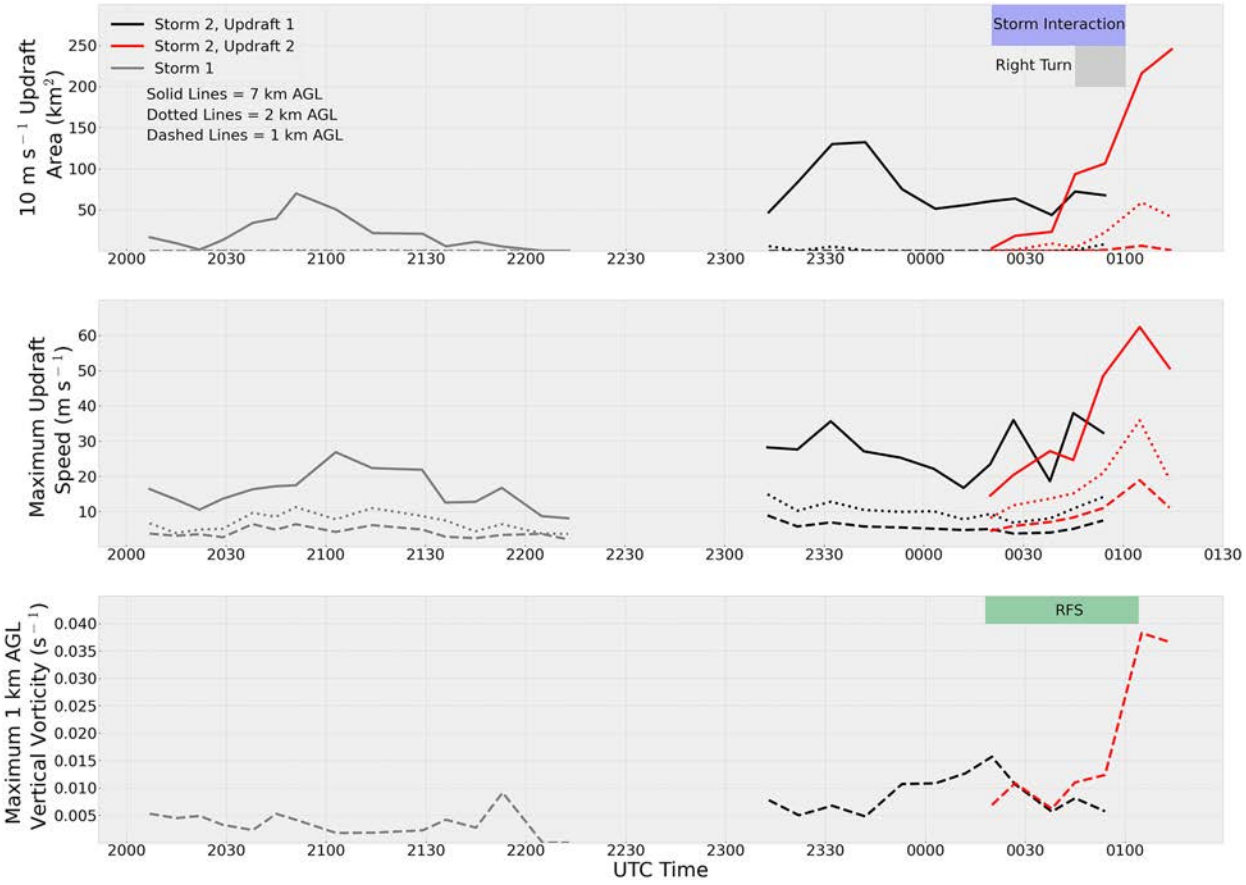

FIG. 5. Time series of (a) 10 m s^{-1} updraft areas at 7 (solid lines), 2 (dotted lines), and 1 km AGL (dashed lines), (b) maximum vertical velocities at the same levels, and (c) maximum 1 km AGL vertical vorticity from P-3 dual-Doppler analyses for both 8 Jun 2019 supercells. For storm 2, values of each quantity are plotted separately for its new and old updrafts during the storm interaction that occurred from 0020 to 0100 UTC. The timing of the storm interaction, sharp right turn, and outflow surge observed with storm 2 are indicated with blue, gray, and green shaded rectangles, respectively.

and little curvature (Fig. 3), which led to 0–2-km storm-relative inflow weaker than the 10 m s^{-1} (19.44 kt) threshold noted by Droegemeier et al. (1993) and Peters et al. (2020) as being favorable for supercells in the 0–3- and 0–2-km layers, respectively (Figs. 7a,b).This weak SR flow and lack of low-level curvature also leads to 0–1-km SRH falling well below the 25th percentile of weakly tornadic events from Thompson et al. (2003) throughout the first supercell's lifetime (Fig. 7d).

Relatively few in situ observations are available for the time between when TORUS left the first supercell and when intensive observations began on the second storm. However, RAP analyses and observations from TORUS after 2330 UTC show that the environment in which the second supercell intensified differed in subtle but important ways from that experienced by the first storm. The TORUS far-field sounding collected at 2357 UTC (Fig. 3) displayed stronger low-level flow, more low-level hodograph curvature, and increased values of SRH and low-level storm-relative flow, especially when calculated with the supercell's motion after its notable right turn after 0000 UTC. In addition, greater boundary layer moisture in this sounding means that the second storm encountered a slightly lower LCL and greater values of MLCAPE than its predecessor. The 0052 UTC far-field sounding (Fig. 3) continues these trends, with stronger low-level storm-relative flow and 0–1-km SRH 2.5 times greater than on the 2357 UTC hodograph, as well as lower LCL heights. While the first storm encountered values of 0–2-km storm-relative flow below the threshold considered favorable by Peters et al. (2020) for supercells, and surface–1-km SRH and MLLCL values unfavorable for tornadoes, by 0052 UTC the second supercell encountered 0–2-km storm-relative flow well above the Peters et al. (2020) threshold, and low-level SRH and MLLCL heights much more favorable for tornadoes (Figs. 7a,b,d). Examining RAP hodographs and 0–1-km SRH across the central Plains (Fig. 8) shows that the changes in the low-level wind profile observed by TORUS occurred across much of western Kansas between 0000 and 0002 UTC 9 June, indicating that the increased low-level SRH experienced by the second supercell was likely a consequence of stronger low-level flow as the boundary layer began to decouple during the EET, rather than an enhancement to the low-level wind fields caused by the supercell itself. These rapid environmental changes likely

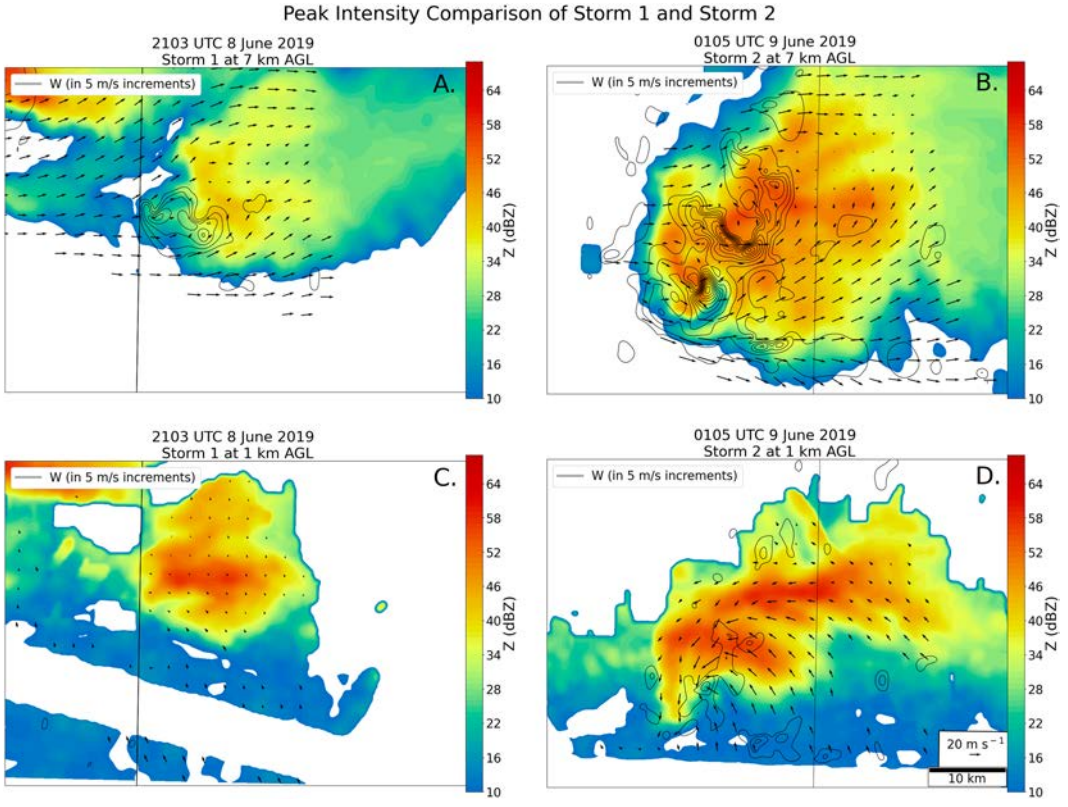

FIG. 6. Dual-Doppler analyses at (a),(b) 7 and (c),(d) 1 km AGL for (left) storm 1 at the time of its maximum 7 km AGL updraft speed and (right) storm 2 at the time of its maximum updraft speed. In each panel, reflectivity is plotted as a color fill, vertical velocities are contoured in black every 5 m s^{-1} starting at 5 m s^{-1}, and horizontal winds are plotted as vectors.

contributed to sustained supercell convection capable of producing tornadoes after 0100 UTC. Examining time series of updraft size (Fig. 5a), maximum vertical velocity (Fig. 5b), and 1 km AGL vertical vorticity (Fig. 5c) shows that the mid- and low-level updrafts of storm 2 markedly expanded and intensified from 0000 to 0100 UTC, and 1 km AGL vertical vorticity values rapidly increased as well. These changes are in line with what would be expected based on the simulations conducted by Coffer and Parker (2015), who found that mid- and low-level mesocyclones strengthened in simulated supercells when they encountered increases in low-level shear and SRH during the EET and that their low-level updrafts intensified due to upward-directed vertical perturbation pressure gradient forces from the strengthening mesocyclones above.

b. *Storm–boundary interactions*

The second 8 June 2019 supercell interacted with two mesoscale boundaries over the course of its life cycle. The first of these boundaries was initially observed in the wake of storm 1 through mobile mesonet transects collected around 2200 UTC (Fig. 9a). This boundary was characterized by cooler temperatures and higher dewpoints to its north, as well as a notable wind shift from southerly south of the boundary to easterly north of the boundary. The increase in moisture to the north of the boundary resulted in a small region where θ_E was higher north of the boundary than in the warmer air to its south. Thus, this boundary may be an example of a mesoscale air mass with high θ_E (MAHTE; Hanft and Houston 2018). Given its location directly behind storm 1, the MAHTE likely

TABLE 1. Table of tornado reports from the second 8 Jun 2019 supercell. EFU denotes tornadoes that are not found to impact any damage indicators and thus cannot be given a rating on the enhanced Fujita scale.

Time (UTC)	Magnitude	NCEI?	Notes
0104–0114	—	No	Several tornado reports from TORUS teams in this window
0157–0201	EFU	Yes	Brief anticyclonic tornado
0210–0226	EFU	Yes	Cyclonic tornado
0305–0307	EFU	Yes	Cyclonic tornado

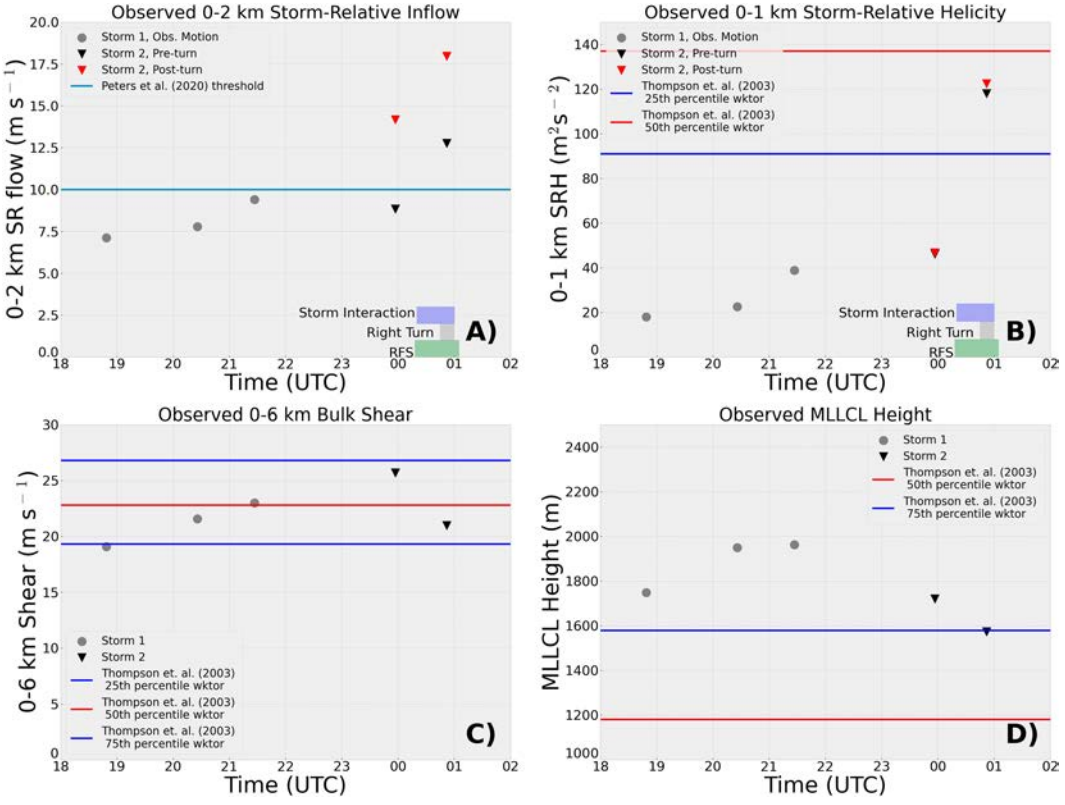

FIG. 7. Time series of observed values of (a) surface–2-km storm-relative flow, (b) surface–1-km storm-relative helicity, (c) surface–6-km bulk shear, and (d) MLLCL height from TORUS far-field soundings on 8 Jun 2019. (a) The storm-relative flow threshold found by Peters et al. (2020) is used to differentiate well between supercells and nonsupercells plotted for reference, and (b)–(d) the median and quartiles of their respective parameters from the weakly tornadic ("wktor") dataset from Thompson et al. (2003) are plotted for comparison. As in Fig. 5, the timing of the storm interaction is marked with a blue box in (a) and (b), storm 2's right turn with a gray box, and the outflow surge with a green box.

originated as modified outflow from storm 1 which began to warm as it emerged into the clearing behind the storm.

A shallow UAS profile was collected by the right flank UAS team as they landed their aircraft just after 2200 UTC within the MAHTE (pink star in Fig. 9), enabling further study of the conditions within the MAHTE. To examine how commonly used convective parameters differ within the MAHTE, data from the UAS sounding were used to replace data from the 2126 UTC far-field sounding from the surface to 850 hPa. At the surface, the lowest-altitude UAS observation was replaced by averaged mobile mesonet observations from within the gray box in Fig. 9, to better represent average surface characteristics within the MAHTE. The resulting composite sounding is plotted alongside the original far-field sounding in Fig. 10. Surface-based CAPE calculated from the composite sounding is 500 J kg^{-1} higher than SBCAPE from the far-field sounding and the LCL is 619 m compared to 2227 m on the far-field sounding. However, surface parcels from within the MAHTE have substantial CINH, with -155 J kg^{-1} compared to the uncapped air mass sampled by the far-field sounding.

The UAS sounding reveals that the MAHTE is extremely shallow, with temperatures and dewpoints nearly returning to the values in the far-field sounding by 100 m AGL. Thus, using a mixed-layer calculation has a major effect on the thermodynamic parameters, with MLCAPE from the composite MAHTE sounding being slightly lower than from the far-field sounding, and the LCL on the composite sounding only being 159 m lower than in the far-field. The shallowness of the MAHTE air mass also may explain why it does not show up on the P-3 dual-Doppler analyses of storm 2 discussed in section 3d, which have limited data in the lowest several hundred meters. Kinematics within the MAHTE air mass also differ from the far-field, with surface–1-km SRH increasing from 39 to 120 m^2 s^{-2} and surface–3-km SRH increasing from 87 to 172 m^2 s^{-2}. Much of this additional shear is also located in the lowest 100 m of the composite sounding. Since UAS observations within the MAHTE are not available between when the rear-flank UAS landed just after 2200 UTC and the second supercell began to track along the edge of the MAHTE around 2300 UTC (Fig. 9b), it is unclear how much mixing modified this air mass before the second supercell interacted with it. If mixing was limited, it is possible that the more-favorable low-level kinematics, lower LCLs, near-surface vertical vorticity, and slightly higher instability within the MAHTE allowed the

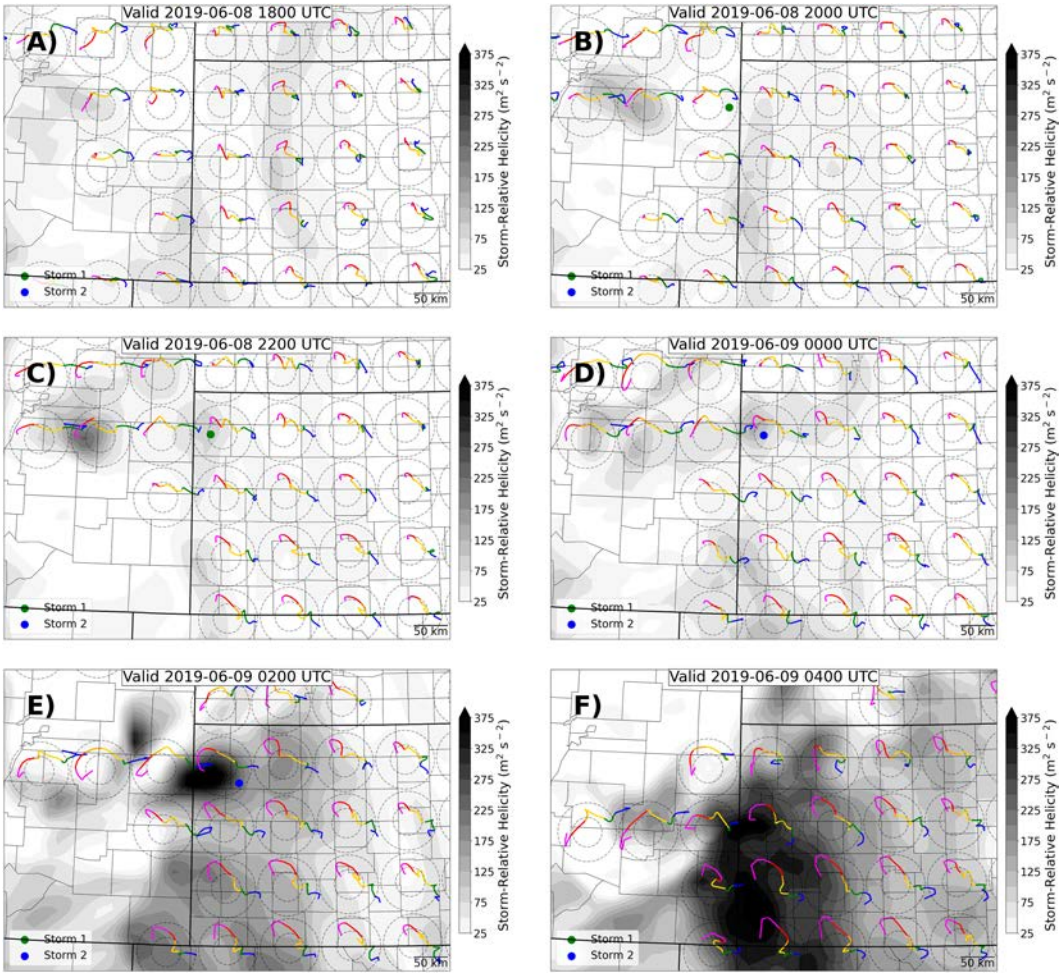

FIG. 8. RAP storm-relative hodographs and surface–3-km storm-relative helicity for 1800 to 0400 UTC 8–9 Jun 2019. Storm-relative hodographs are plotted using Bunkers et al.'s (2000) storm motions, and segments on the hodographs are colored as follows: surface–1 km (magenta), 1–2 km (red), 2–3 km (orange), 3–6 km (yellow), 6–9 km (blue), and 9–12 km (green). Storm locations are marked with green (storm 1) and blue (storm 2) dots.

second supercell to intensify and develop a strong low-level mesocyclone more quickly than it would have if that MAHTE had not been present. However, since we do not have observations to determine how much the MAHTE air mass was modified between 2200 and 2300 UTC, it must be stressed that this is just one possible hypothesis about how this interaction may have played out. It is also possible that the MAHTE did not destabilize enough to be ingested into the inflow of storm 2, or conversely that much of the moisture and more-favorable kinematics within the MAHTE was mixed out if more destabilization occurred.

The second boundary which interacted with storm 2 approached from the NW and interacted with storm 2 between 2300 and 0000 UTC. It was observed as a fine line and wind shift on base velocity data from KGLD and originated as outflow from a cluster of cells near St. Francis, Kansas, around 2200 UTC (Fig. 11a). As it began to interact with the developing storm 2 around 2300 UTC (Fig. 11b), it stalled out oriented southwest–northeast with the southwest portion of the boundary extending toward the developing supercell's updraft (Fig. 11b). The boundary then maintained this storm-relative position while being absorbed into storm 2's cold pool (Figs. 11c,d). By 2346 UTC, the convergence associated with the boundary has been replaced by divergence within storm 2's cold pool (Fig. 11d). Besides this boundary's evolution on radar, little is known about its thermodynamic or kinematic characteristics, since the TORUS armada did not sample this boundary directly. Thus, we cannot assess whether this boundary would have provided additional baroclinic streamwise vorticity or vertical vorticity to strengthen the low-level mesocyclone of storm 2.

c. *Differences in deep convection initiation*

Visual observations from the field of the 8 June 2019 supercells showed that the first storm had a relatively narrow updraft with a ragged appearance, indicating that it may have been struggling with entrainment while TORUS was observing it (Fig. 12a). In contrast, visual observations from the TORUS

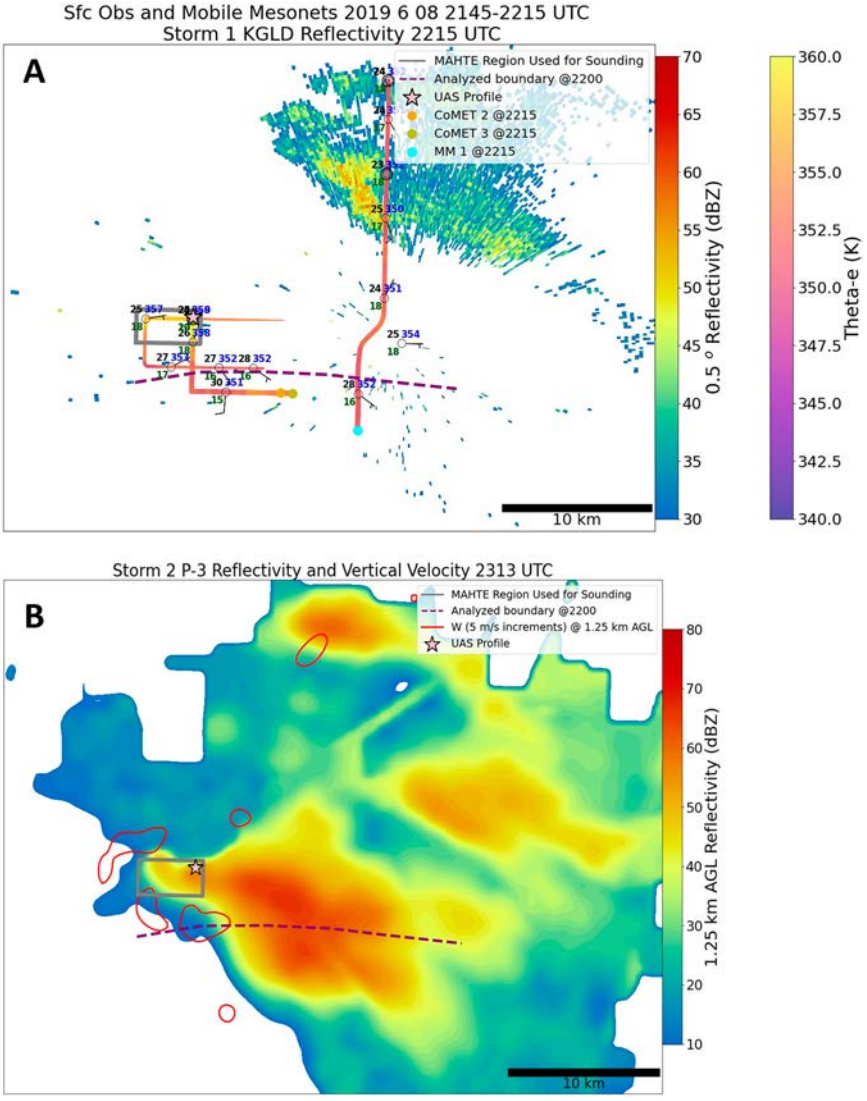

FIG. 9. Maps showing (a) mobile mesonet data from 2145 to 2215 UTC as TORUS sampled the MAHTE air mass and KGLD radar data from 2215 UTC, along with the manually analyzed outflow boundary at 2200 UTC and (b) P-3 TDR reflectivity and vertical velocity from 2313 UTC at 1.25 km AGL. In (a), mobile mesonet transects are colored by equivalent potential temperature and the thickness of the plotted mobile mesonet data decreases with increasing time after 2215 UTC. Station plots along the mobile mesonet traces are plotted from mobile mesonet data and are thinned for readability, with temperature plotted in black, dewpoint in green, and equivalent potential temperature in blue. A station plot for the closest KGLD observation to 2200 UTC is also shown. All temperature and dewpoint values are in degrees Celsius. In (b), the 2200 UTC boundary location, MAHTE region, and UAS sounding location are marked as in (a).

teams approaching storm 2 from the south at 2325 UTC show several indications that it had a broader updraft and was struggling less with entrainment than storm 1, including a markedly crisper updraft, a notably back-sheared anvil, and a broad rain-free base (Fig. 12b). Since the second storm's initiation and early evolution occurred almost exactly where the first storm had tracked previously, this difference may in part be due to preconditioning of the second storm's environment by detrained moisture from the first storm, which would make entrainment less impactful for the second storm.

It was also hypothesized that storm 2 developed from a larger, more vigorous area of initial CI than storm 1 and that its larger initial updraft allowed it to better resist entrainment and allowed it to become stronger and deviate further to the right, as in the results of Flournoy and Rasmussen (2023). To test this hypothesis, an attempt was made to use overshooting

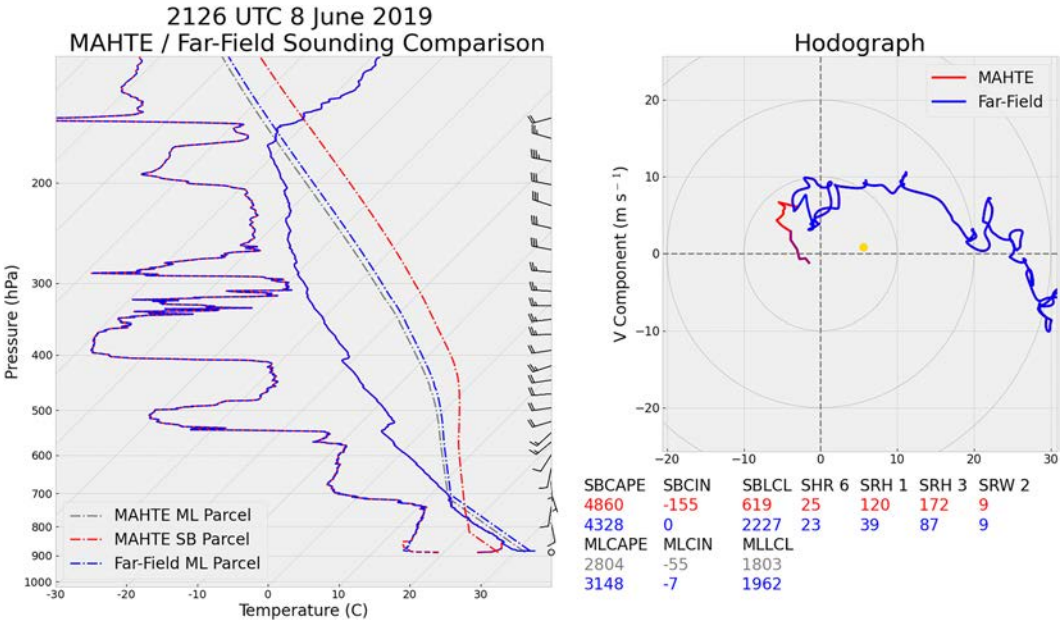

FIG. 10. Comparison of the 2126 UTC TORUS far-field sounding with a composite sounding created by replacing the data from the surface up to 850 hPa on the far-field sounding with data collected by the rear-flank UAS as it descended into the MAHTE. The original far-field sounding, hodograph, and parcel profile are plotted in blue, and the same things are plotted in red for the composite sounding. Where the two soundings overlap exactly, the blue far-field sounding is shown. Surface conditions on the composite sounding were obtained by averaging mobile mesonet observations within the gray box enclosing the core of the MAHTE in Fig. 9. Sections of the composite sounding and hodograph below 100 m AGL are colored purple. Mixed-layer (ML) parcels in this figure are created by mixing the lowest 50 hPa of a given profile, and the mixed-layer parcel profile for the composite sounding is plotted in green.

top areas and Z_{DR} columns as proxies for initial updraft size for both storms, since dual-Doppler analyses created from the NOAA P-3 TDR data were not available until 30 min after CI. Unfortunately, the top of storm 2 was obscured by anvil cirrus from the remnants of storm 1 during its initial development, and the close proximity of storm 2 to the Goodland, Kansas, WSR-88D site around CI meant that its Z_{DR} column was above the radar's highest tilts. Thus, the lack of usable observational proxies for both storm's initial updrafts unfortunately prevented a robust comparison of their sizes and strengths.

d. *Storm interactions*

From 0020 to 0100 UTC, storm 2 underwent an interaction with a new updraft which developed over its rear-flank outflow, rapidly intensified as it dove southeastward, and took over as the primary updraft by 0105 UTC (Fig. 13). New updrafts and associated echoes first appeared west of storm 2 on dual-Doppler analyses constructed using data from the NOAA P-3's tail Doppler radars at 0012 UTC (Fig. 13a), and by 0027 UTC, a strong new updraft is analyzed west of storm 2 (Fig. 13b). Between 0027 and 0045 UTC, this new updraft rapidly intensifies and dives southeast, while the original updraft maintains its intensity and slowly drifts eastward (Fig. 13c). By 0054 UTC, the new updraft displays a prominent bounded weak echo region (BWER) (Fig. 13d) and has surpassed the old updraft in strength, with maximum vertical velocities between 40 and 50 m s^{-1} compared to 30 m s^{-1} in the original updraft. Moreover, precipitation from the new updraft, if transported to the east-northeast by the mean wind, would be falling near the location of the old updraft at this time. By 0114 UTC, the new updraft has become dominant and the old updraft has nearly dissipated (Figs. 13d,f).

In the lower levels, the changes observed during this interaction are even more dramatic. Prior to the interaction, storm 2's low-level (1 km AGL) mesocyclone appeared relatively weak and disorganized, with no well-defined area of strong vertical velocities or strong vertical vorticity at 1 km AGL (Figs. 14a,b and 15a,b). At 0045 UTC, a better-defined area of convergence has developed below the midlevel updraft, and vertical velocities there increase as the storm dives southeast by 0054 UTC (Figs. 14c,d and 15c,d). By 0105 UTC, a well-defined mesocyclone has emerged at 1 km AGL, with a compact circulation collocated with vertical velocities of up to 15 m s^{-1} (Figs. 14e and 15e). A tight low-level couplet also appears on KGLD velocity at 0104 UTC (not shown). Around this time, several members of the TORUS team reported brief tornadoes (http://catalog.eol.ucar.edu/torus_2019/reports), and video footage taken by the Texas Tech Ka radar teams shows dust whirls beneath the low-level mesocyclone (A. Schueth 2020, personal communication). However, the NCEI Storm Events Database (https://www.ncdc.noaa.gov/stormevents/) does not note a tornado at this point.

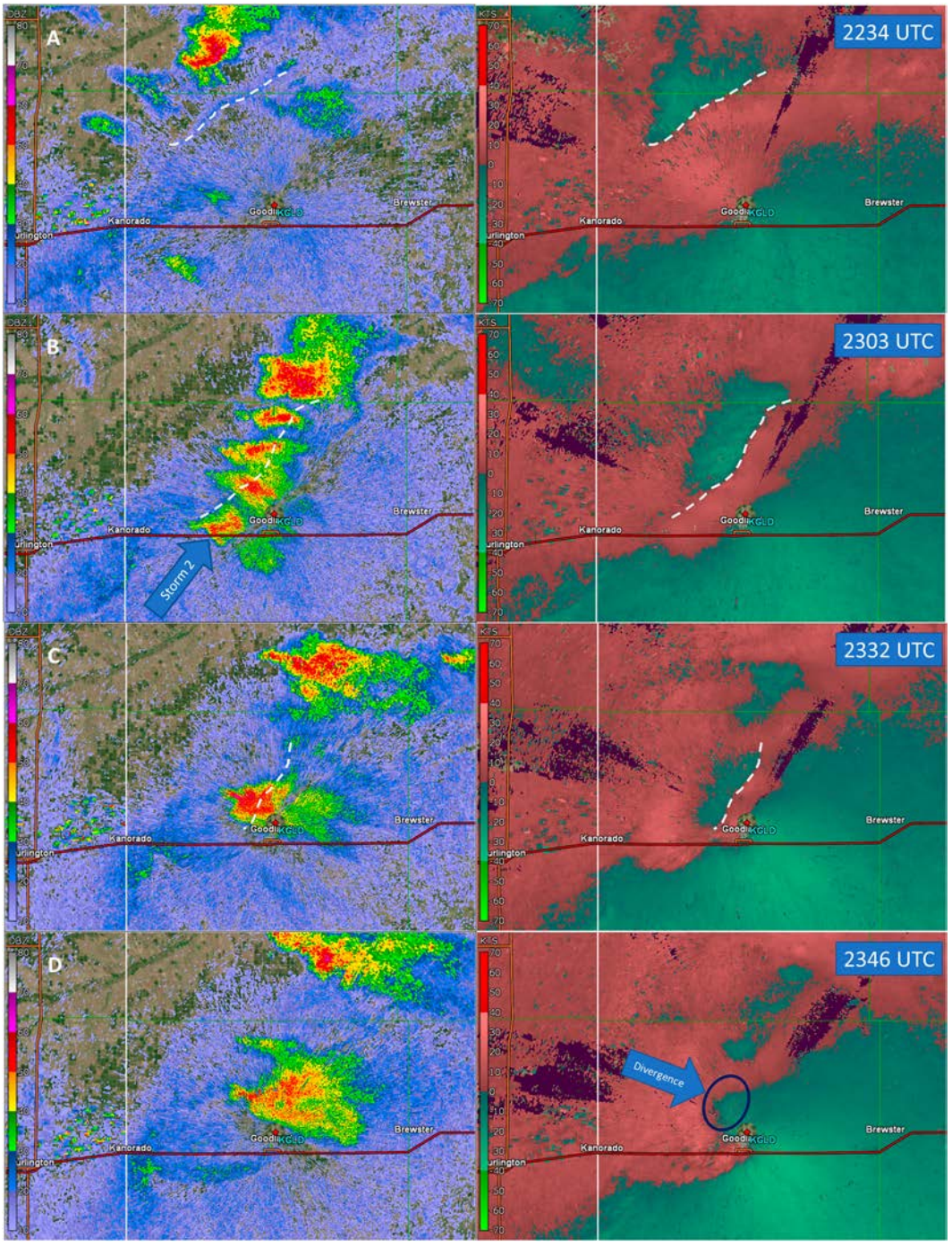

FIG. 11. (left) Radar reflectivity (dBZ) and (right) storm-relative velocity (kt) for the second 8 Jun 2019 supercell at (a) 2234, (b) 2303, (c) 2332, and (d) 2346 UTC. The white dashed lines on the velocity images and white dashed lines on the reflectivity images represent the third boundary discussed above.

The low-level mesocyclone weakens somewhat on the 0114 UTC dual-Doppler analysis (Fig. 14f), and it is not until 0157 UTC that NCEI records the next tornado from storm 2 (a brief anticyclonic tornado near Winona, Kansas) and 0210 UTC that it produces its next cyclonic tornado.

While the changes in storm 2 observed during this interaction were impressive, it is important to note that these changes were also occurring during the EET as low-level shear and SRH rapidly increased (Figs. 7a,b), leading to an increased likelihood of a given supercell present in that environment intensifying and

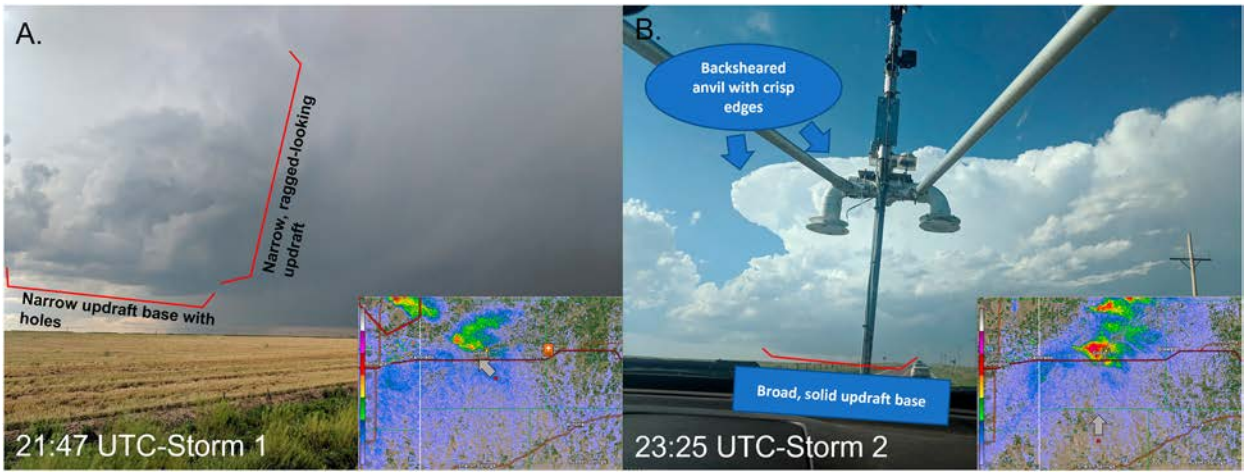

FIG. 12. Photographs of (a) the first 8 Jun 2019 supercell at 2147 UTC from the near inflow mission location and (b) the second 8 Jun 2019 supercell at 2325 UTC as the near inflow team was approaching the storm from the south.

becoming tornadic. Thus, it is possible that a marked increase in the intensity of the mid- and low-level mesocyclones of storm 2 would have occurred without this interaction over the same time frame, or that the observed intensification of the new updraft as it interacted with the old updraft of storm 2 is just the intensification which would be expected from a new supercell updraft developing in this increasingly favorable environment.

e. *Internal storm processes*

Within storm 2, an outflow surge was noted on KGLD imagery, which may have played a role in both the rapid formation and intensification of the new updraft discussed in section 3d and the rightward deviation of the new updraft and the storm after the merger. This surge may originate in part from outflow (visible as a fine line on KGLD imagery in Fig. 16a) that emerges from a small cell which appears to be a short-lived left split[1] on the northern flank of storm 2 around 0018 UTC. This surge appeared superficially similar to a rear-flank internal surge (RFIS; Skinner et al. 2014; Lee et al. 2012); however, it does not quite meet the definition of an RFIS since it does not originate entirely from within the ongoing rear-flank downdraft. Between 0020 and 0029 UTC, this outflow rapidly expands and passes beneath the developing new updraft to the west of storm 2, possibly providing additional low-level convergence to encourage its rapid strengthening and deviant southeast propagation (Fig. 16b). By 0035 UTC, the outflow surge has caught up with the leading rear-flank gust front (RFGF) and is located beneath the southeast-diving new updraft, as seen in Fig. 16c. Between 0035 and 0104 UTC, the primary RFGF west of the new updraft surges southward while the section of the boundary beneath the updraft becomes anchored to the updraft, creating a cusp along the boundary at the location of the low-level mesocyclone (Fig. 16d). As the boundary continues to surge southward, storm 2 takes on the deviant southeast motion of the dominant new updraft. By encouraging this deviant motion, the outflow surge may have helped storm 2 take better advantage of its improving environment by allowing it to experience stronger storm-relative inflow and higher SRH than it would have without the deviant southeast motion (Figs. 7a,b).

[1] While interaction with an outflow surge from convection in the process of becoming a left split may be considered a storm interaction rather than an internal process, since at the time the outflow surge originates the reflectivity footprint of the nascent left split still substantially overlaps that of storm 2, we consider it to be at most incompletely split from the main supercell. Thus, we consider this outflow to be an internal process.

4. Conclusions

In this work, we have used data from the TORUS project to examine why, despite being located in close spatial and temporal proximity, the two supercells observed during the 8 June 2019 TORUS IOP evolved quite differently. In our analysis, we focused on five potential factors which prior work indicated may account for differences between proximate storms: rapid temporal evolution of the environment, spatial heterogeneities in environmental conditions, differences in deep convection initiation between storms, storm interactions, and internal storm processes. Our main findings are as follows (Fig. 17):

1) The environment evolved rapidly between the demise of storm 1 and the tornadic phase of storm 2 to become more favorable for tornadogenesis, with storm 2 experiencing low-level hodographs with greater curvature, more shear and SRH, and lower LCLs than storm 1. Given the magnitude of these changes and the importance of these parameters for low-level mesocyclone and tornado formation, we have relatively high confidence that these rapid temporal changes in the environment played an important role in the differences between the two 8 June supercells and raised the probability of storm 2 becoming tornadic.
2) Storm 2 encountered two preexisting airmass boundaries that storm 1 did not interact with. The first of these boundaries was formed from rapidly modifying outflow behind storm 1 and contained higher equivalent potential temperature, lower LCLs, and larger low-level SRH than

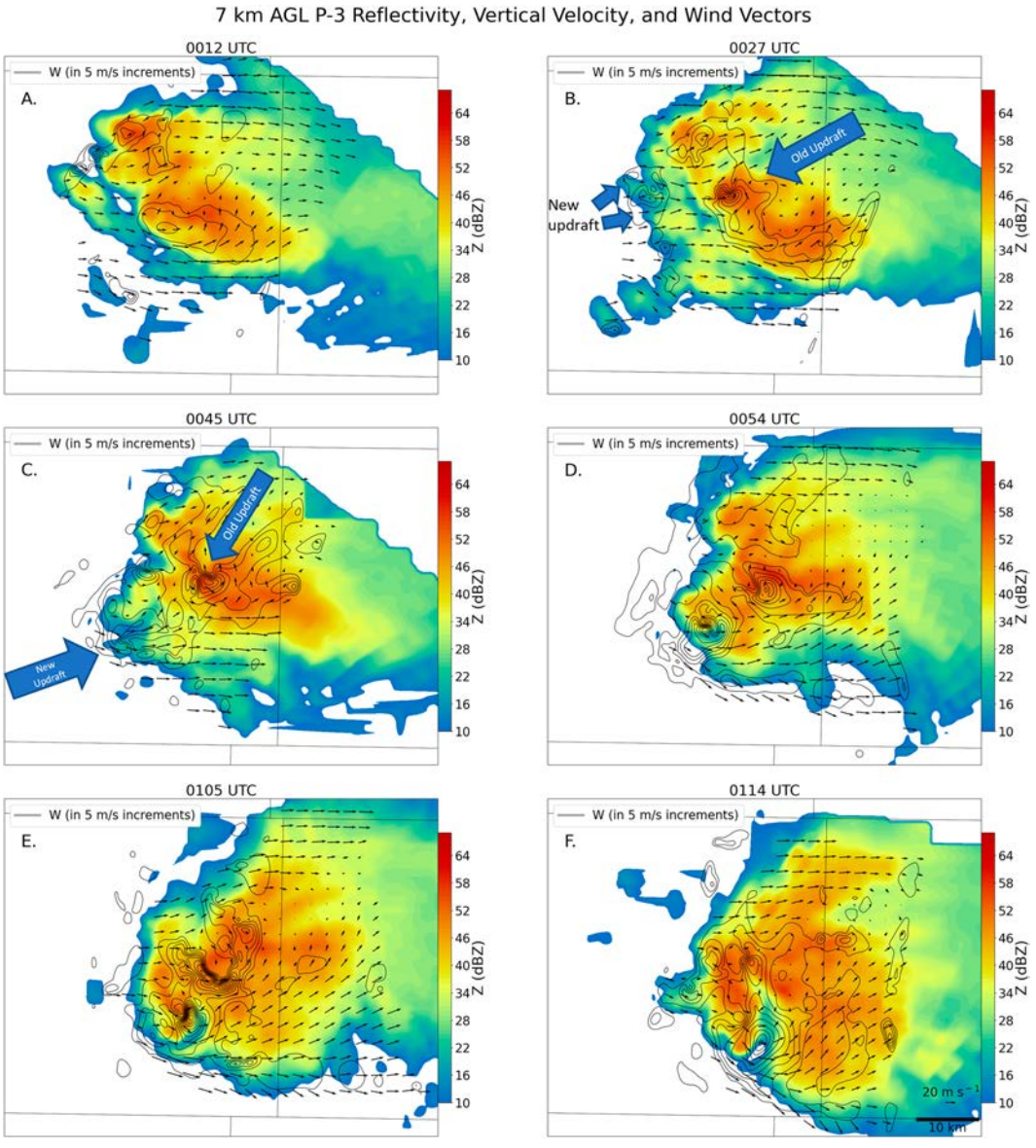

FIG. 13. P-3 dual-Doppler analyses at 7 km AGL from (a) 0012, (b) 0027, (c) 0045, (d) 0054, (c) 0105, and (d) 0114 UTC. Each panel shows reflectivity, dual-Doppler vertical velocities (contoured every 5 m s^{-1} starting at 5 m s^{-1}), and horizontal wind vectors.

air in the undisturbed environment to its south. However, it was very shallow and included a fairly strong low-level inversion, so the effect of this air mass on storm 2 likely depended on how it evolved storm before 2 arrived. Unfortunately, we do not have measurements within this air mass between TORUS's departure from the storm just after 2200 UTC and storm 2's arrival to determine how it evolved during this time. Storm 2 also encountered a second boundary which originated as outflow from cells to the north and interacted with storm 2's precipitation core as it was rapidly developing between 2303 and 2346 UTC. This boundary was not sampled by TORUS assets. Thus, little can be said about its characteristics or whether it provided additional baroclinic streamwise vorticity or vertical vorticity to aid in the intensification of storm 2. Overall, given the lack of in situ observations of these boundaries just before or during their interactions with storm 2, we have less confidence in what the impact of each boundary was compared to the rapid environmental changes discussed above.

3) Although storm 2's initial updraft visually appeared larger and more intense than that of storm 1, the limitations of the available observations in this case prevented a definitive determination of whether storm 2 emerged from a larger, more vigorous area of deep convection initiation.

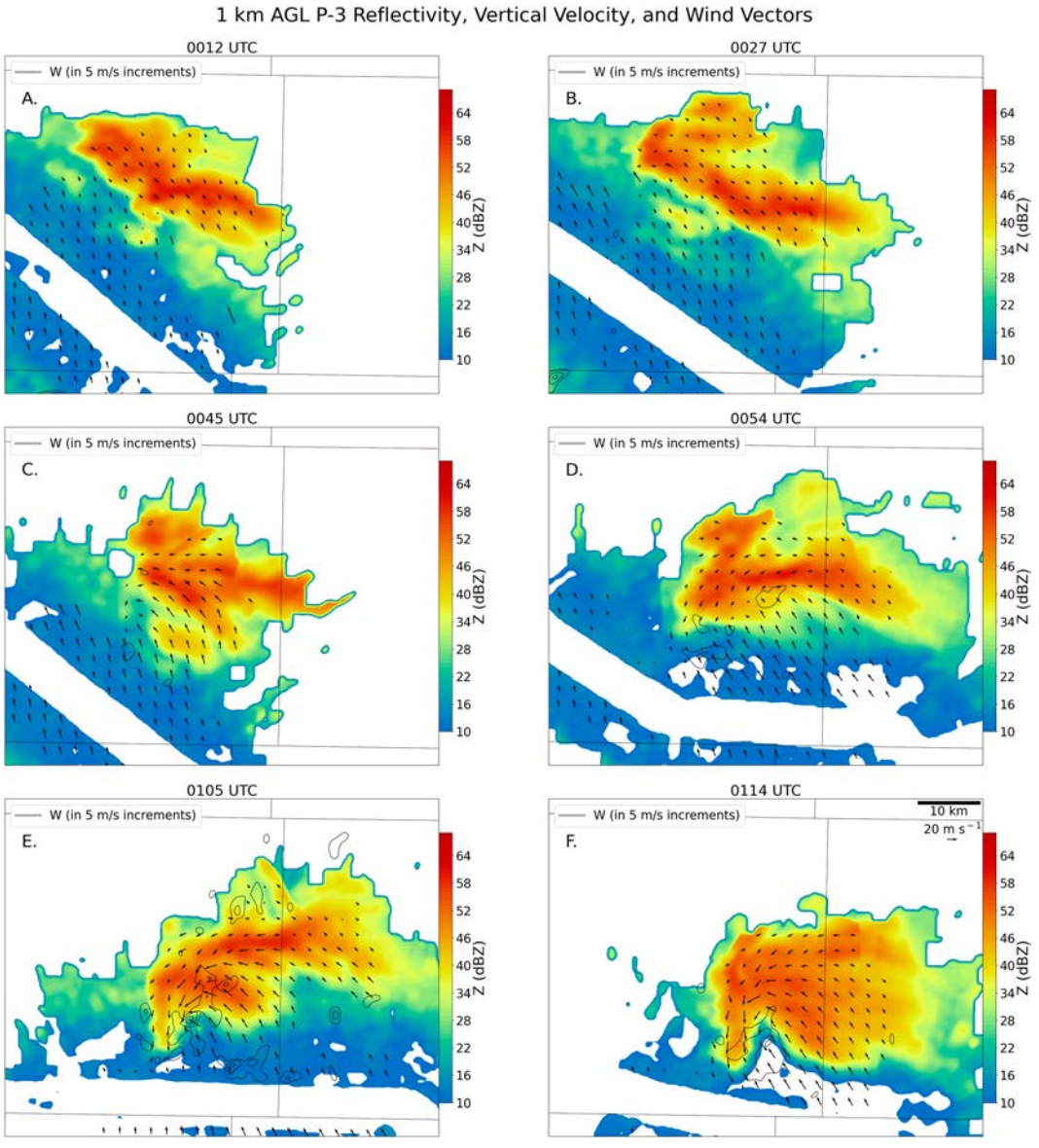

FIG. 14. P-3 dual-Doppler analyses at 1 km AGL from (a) 0012, (b) 0027, (c) 0045, (d) 0054, (c) 0105, and (d) 0114 UTC. Each panel shows reflectivity, dual-Doppler vertical velocities (contoured every 5 m s^{-1} starting at 5 m s^{-1}), and horizontal wind vectors.

4) Storm 2 interacted with a new updraft that formed on its right flank, rapidly intensified and deviated rightward, and took over as the primary updraft of storm 2 by 0054 UTC. This interaction resulted in a much stronger midlevel updraft and low-level mesocyclone than were present beforehand. While it is unknown whether storm 2 would have ended up undergoing a similar process of intensification without this interaction, given prior work (Rogers and Weiss 2008; Hastings and Richardson 2016; Fischer and Dahl 2022) that has found a propensity for rear-flank mergers to precede tornadogenesis compared to mergers elsewhere, and the stark difference in the structure of storm 2 before and after this interaction, we have relatively high confidence that this interaction made it stronger and more likely to produce a tornado than it would have been otherwise.
5) Just before and during the aforementioned interaction, a notable outflow surge was observed sweeping around the western side of storm 2. This outflow surge originated in a section of storm 2 that was splitting from the main storm to become a short-lived left-moving supercell, and swept beneath the developing rear-flank cell just before it rapidly intensified and merged with storm 2, possibly assisting the new updraft's development with additional low-level convergence. In addition, the marked rightward deviation of the new updraft (and storm 2 as a whole) began in

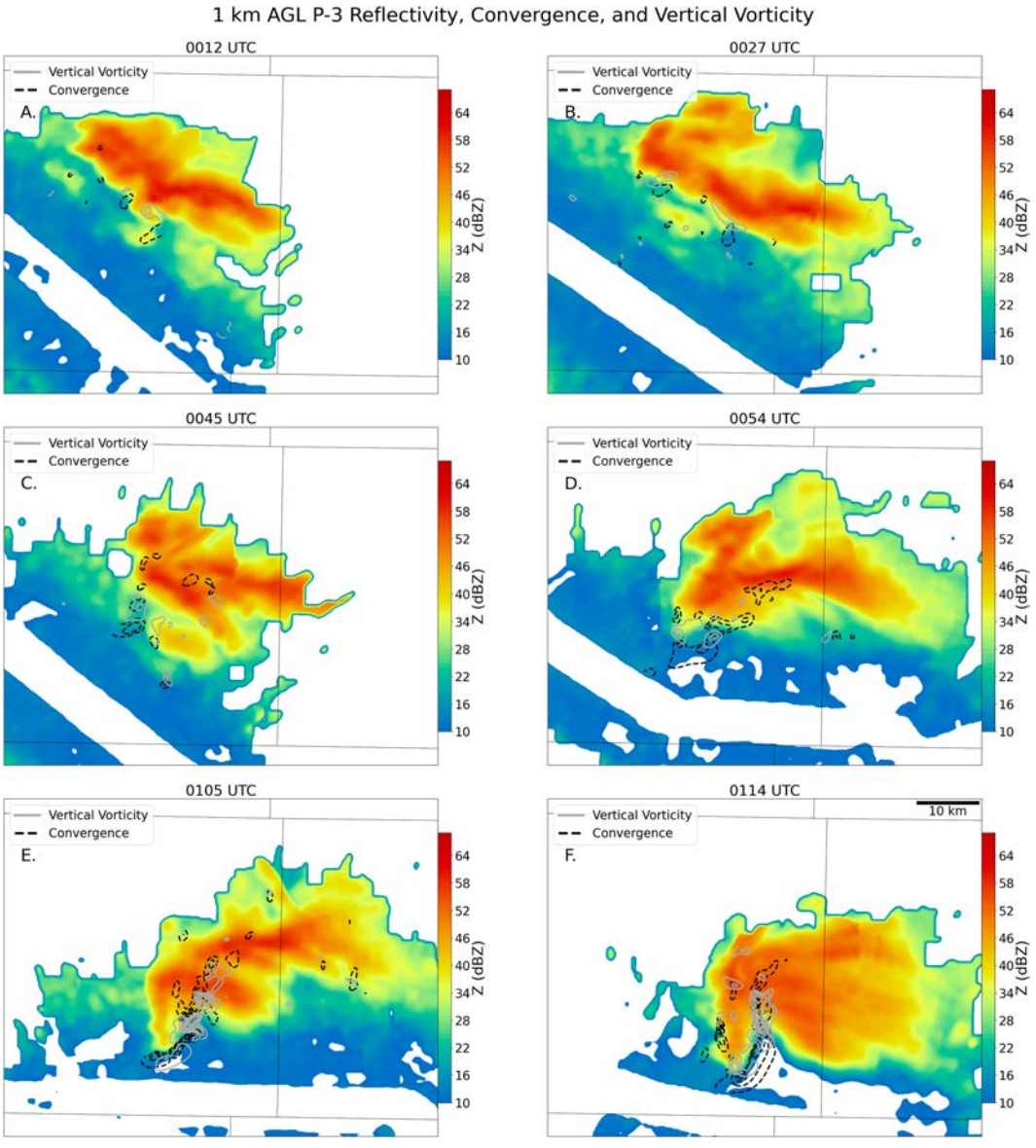

FIG. 15. P-3 dual-Doppler analyses at 1 km AGL from (a) 0012, (b) 0027, (c) 0045, (d) 0054, (c) 0105, and (d) 0114 UTC. Each panel shows vertical vorticity (contoured in gray every 0.005 s^{-1} starting at 0.005 s^{-1}) and convergence (contoured in dashed black every 0.005 s^{-1} starting at 0.005 s^{-1}).

tandem with this outflow surge wrapping around the rear of the storm and may have been influenced by propagation of the new updraft to the southwest along this boundary. Given the changes associated with the passage of this outflow surge, we have relatively high confidence it played a role in storm 2's intensification and raised its probability of producing a tornado.

The results presented here provide evidence (albeit from one case) for several ways that environmental heterogeneities or storm-scale processes can impact a given supercell's likelihood of becoming tornadic. Storm 2 had notably more deviant motion than storm 1, consistent with the observed tendency for tornadic supercells to deviate more to the right than their nontornadic neighbors (Bunkers et al. 2022). It survived long enough to experience a rapidly improving low-level shear profile later in the evening while its counterpart did not (e.g., Klees et al. 2016). Finally, it experienced a constructive storm interaction resembling a rear-flank merger, which is more likely to lead to intensification compared to mergers in other storm quadrants (e.g., Rogers and Weiss 2008; Hastings and Richardson 2016).

Our analysis also highlights the need for denser, more frequent observations in severe storm environments. For example, the shallowness of the MAHTE on the cool side of the first boundary would have been difficult to ascertain without data above the surface from UAS, and without TORUS data,

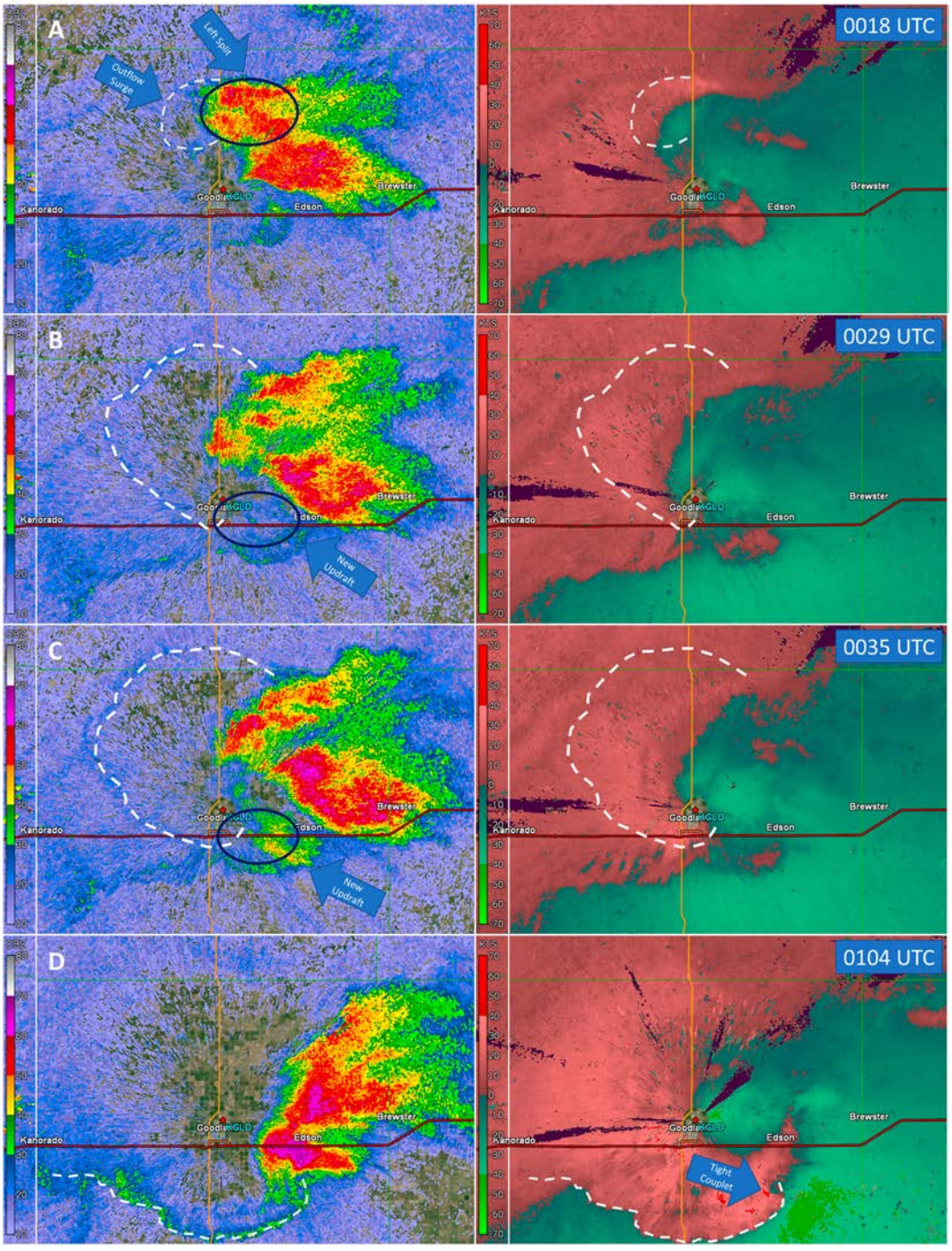

FIG. 16. (left) Radar reflectivity (dBZ) and (right) storm-relative velocity (kt) for the second 8 Jun 2019 supercell at (a) 0018, (b) 0029, (c) 0035, and (d) 0104 UTC. The white dashed line represents the edge of the outflow surge discussed above.

its presence may have gone unnoticed entirely. In situ observations of the second mesoscale boundary could have also allowed for a better characterization of its impacts on storm 2, and more-favorably placed WSR-88D observations would have allowed for an estimate of each storm's initial updraft size using Z_{DR} columns. Future work by the lead authors involving this case will focus on assimilating TORUS data into a storm-scale ensemble to determine if it improves the model's ability to represent some of these mesoscale features and the resulting short-term ensemble forecasts.

Finally, none of the mesoscale influences which led to the differences between the first and second 8 June 2019 supercells

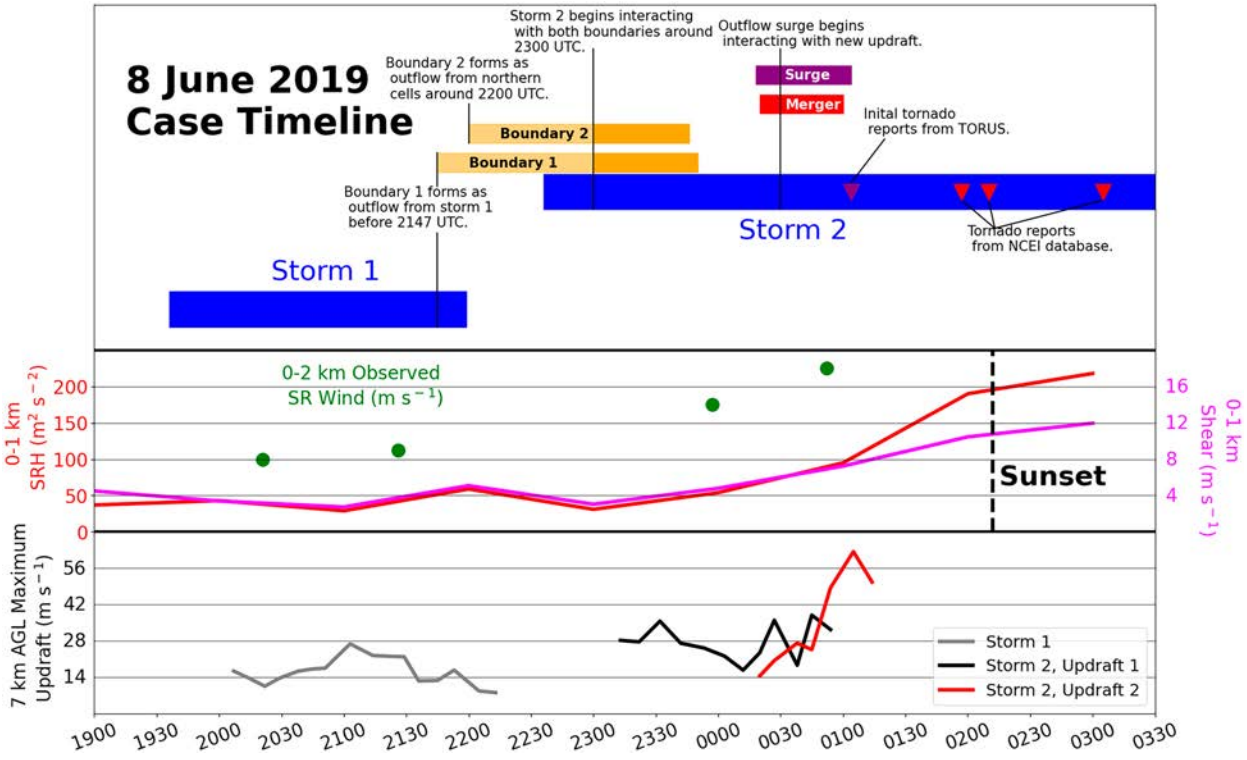

FIG. 17. Timeline summarizing the important events in the life cycles of storms 1 and 2. The blue bars labeled "storm 1" and "storm 2" cover each storm's life cycle from CI to dissipation (or the end of the observing period in the case of storm 2). The orange bars for boundary 1 and boundary 2 denote the full time each boundary could be noted in available in situ or radar observations. Surface–1-km shear and SRH time series are from RAP analysis soundings from Russell Springs, KS (60 km south-southeast of storm 2 at 0100 UTC), and observed 0–2-km storm-relative winds are plotted as green dots on the same axis as the 0–1-km shear. Updraft intensities are from the P-3 dual-Doppler analyses discussed earlier.

operated in isolation from each other. Rather, they often overlapped in time and space (Fig. 17), and interactions between them may have played an important role in the evolution of storm 2. A larger initial updraft on storm 2 may have allowed it to better take advantage of its interactions with the two mesoscale boundaries in its environment and may have primed it for a more favorable outcome from the cell interaction it underwent after 0000 UTC. The rapidly intensifying new updraft that interacted with storm 2 between 0020 and 0100 UTC before becoming the primary updraft may have been enhanced by convergence from the strong outflow surge which swept beneath it beginning around 0030 UTC. The production of this outflow surge may have been more likely with storm 2's larger initial updraft, which may have been further enhanced by its interaction with the two mesoscale boundaries. Finally, all of these interactions occurred as the near-storm environment was rapidly changing, with a rapid increase in low-level SRH and storm-relative flow making conditions more favorable for strong low-level mesocyclones and tornadoes, and also possibly making conditions more favorable for these interactions to result in intensification of storm 2. Further work examining how interactions between environmental heterogeneities, rapid environmental changes, cell interactions, and internal storm processes influence storm evolution (especially involving numerical simulations combining two or more of these elements) would be helpful in better understanding cases like this where proximate storms have very different evolutions and outcomes.

Acknowledgments. The authors thank the TORUS team for their work collecting the data used in this paper. We would also like to thank Dr. Casey Davenport, Dr. Brice Coffer, and one anonymous reviewer for their helpful comments, which improved this manuscript. Authors Wilson and Houston would like to acknowledge funding from the NSF-TORUS Grant (AGS-1824649). Dr. Cameron Nixon is acknowledged for providing the hodograph map code.

Data availability statement. The TORUS datasets used in this paper are available at https://www.eol.ucar.edu/field_projects/torus.

REFERENCES

Alford, A. A., M. I. Biggerstaff, C. L. Ziegler, D. P. Jorgensen, and G. D. Carrie, 2022: A method for correcting staggered pulse repetition time (PRT) and dual pulse repetition frequency (PRF) processor errors in research radar datasets. *J. Atmos. Oceanic Technol.*, **39**, 1763–1780, https://doi.org/10.1175/JTECH-D-21-0176.1.

Atkins, N. T., M. L. Weisman, and L. J. Wicker, 1999: The influence of preexisting boundaries on supercell evolution. *Mon. Wea. Rev.*, **127**, 2910–2927, https://doi.org/10.1175/1520-0493(1999)127<2910:TIOPBO>2.0.CO;2.

Barnes, S. L., 1964: A technique for maximizing details in numerical weather map analysis. *J. Appl. Meteor.*, **3**, 396–409, https://doi.org/10.1175/1520-0450(1964)003<0396:ATFMDI>2.0.CO;2.

Benjamin, S. G., and Coauthors, 2016: A North American hourly assimilation and model forecast cycle: The Rapid Refresh. *Mon. Wea. Rev.*, **144**, 1669–1694, https://doi.org/10.1175/MWR-D-15-0242.1.

Bluestein, H. B., and M. L. Weisman, 2000: The interaction of numerically simulated supercells initiated along lines. *Mon. Wea. Rev.*, **128**, 3128–3149, https://doi.org/10.1175/1520-0493(2000)128<3128:TIONSS>2.0.CO;2.

Blumberg, W. G., K. T. Halbert, T. A. Supinie, P. T. Marsh, R. L. Thompson, and J. A. Hart, 2017: SHARPpy: An open-source sounding analysis toolkit for the atmospheric sciences. *Bull. Amer. Meteor. Soc.*, **98**, 1625–1636, https://doi.org/10.1175/BAMS-D-15-00309.1.

Brooks, H. E., and R. B. Wilhelmson, 1992: Numerical simulation of a low-precipitation supercell thunderstorm. *Meteor. Atmos. Phys.*, **49**, 3–17, https://doi.org/10.1007/BF01025398.

Brown, M. C., C. J. Nowotarski, A. R. Dean, B. T. Smith, R. L. Thompson, and J. M. Peters, 2021: The early evening transition in southeastern U.S. tornado environments. *Wea. Forecasting*, **36**, 1431–1452, https://doi.org/10.1175/WAF-D-20-0191.1.

Bunkers, M. J., B. A. Klimowski, J. W. Zeitler, R. L. Thompson, and M. L. Weisman, 2000: Predicting supercell motion using a new hodograph technique. *Wea. Forecasting*, **15**, 61–79, https://doi.org/10.1175/1520-0434(2000)015⟨0061:PSMUAN⟩2.0.CO;2.

——, M. B. Wilson, M. S. Van Den Broeke, and D. J. Healey, 2022: Scan-by-scan storm-motion deviations for concurrent tornadic and nontornadic supercells. *Wea. Forecasting*, **37**, 749–770, https://doi.org/10.1175/WAF-D-21-0153.1.

Coffer, B. E., and M. D. Parker, 2015: Impacts of increasing low-level shear on supercells during the early evening transition. *Mon. Wea. Rev.*, **143**, 1945–1969, https://doi.org/10.1175/MWR-D-14-00328.1.

——, and ——, 2017: Simulated supercells in nontornadic and tornadic VORTEX2 environments. *Mon. Wea. Rev.*, **145**, 149–180, https://doi.org/10.1175/MWR-D-16-0226.1.

——, ——, J. M. L. Dahl, L. J. Wicker, and A. J. Clark, 2017: Volatility of tornadogenesis: An ensemble of simulated nontornadic and tornadic supercells in VORTEX2 environments. *Mon. Wea. Rev.*, **145**, 4605–4625, https://doi.org/10.1175/MWR-D-17-0152.1.

——, ——, R. L. Thompson, B. T. Smith, and R. E. Jewell, 2019: Using near-ground storm relative helicity in supercell tornado forecasting. *Wea. Forecasting*, **34**, 1417–1435, https://doi.org/10.1175/WAF-D-19-0115.1.

Coniglio, M. C., and M. D. Parker, 2020: Insights into supercells and their environments from three decades of targeted radiosonde observations. *Mon. Wea. Rev.*, **148**, 4893–4915, https://doi.org/10.1175/MWR-D-20-0105.1.

Craven, J. P., and H. E. Brooks, 2004: Baseline climatology of sounding derived parameters associated with deep moist convection. *Natl. Wea. Dig.*, **28**, 13–24.

Davenport, C. E., 2021: Environmental evolution of long-lived supercell thunderstorms in the Great Plains. *Wea. Forecasting*, **36**, 2187–2209, https://doi.org/10.1175/WAF-D-21-0042.1.

——, and M. D. Parker, 2015: Impact of environmental heterogeneity on the dynamics of a dissipating supercell thunderstorm. *Mon. Wea. Rev.*, **143**, 4244–4277, https://doi.org/10.1175/MWR-D-15-0072.1.

Droegemeier, K. K., S. M. Lazarus, and R. Davies-Jones, 1993: The influence of helicity on numerically simulated convective storms. *Mon. Wea. Rev.*, **121**, 2005–2029, https://doi.org/10.1175/1520-0493(1993)121<2005:TIOHON>2.0.CO;2.

Fischer, J., and J. M. L. Dahl, 2022: Supercell-external storms and boundaries acting as catalysts for tornadogenesis. *Mon. Wea. Rev.*, **151**, 23–38, https://doi.org/10.1175/MWR-D-22-0026.1.

Flournoy, M. D., and E. N. Rasmussen, 2023: The influence of convection initiation strength on subsequent simulated supercell evolution. *Mon. Wea. Rev.*, **151**, 2179–2203, https://doi.org/10.1175/MWR-D-22-0069.1.

——, M. C. Coniglio, E. N. Rasmussen, J. C. Furtado, and B. E. Coffer, 2020: Modes of storm-scale variability and tornado potential in VORTEX2 near- and far-field tornadic environments. *Mon. Wea. Rev.*, **148**, 4185–4207, https://doi.org/10.1175/MWR-D-20-0147.1.

——, A. W. Lyza, M. A. Satrio, M. R. Diedrichsen, M. C. Coniglio, and S. Waugh, 2022: A climatology of cell mergers with supercells and their association with mesocyclone evolution. *Mon. Wea. Rev.*, **150**, 451–461, https://doi.org/10.1175/MWR-D-21-0204.1.

Frew, E., B. Argrow, S. Borenstein, S. Swenson, C. A. Hirst, H. Havenga, and A. Houston, 2020: Field observation of tornadic supercells by multiple autonomous fixed-wing unmanned aircraft. *J. Field Rob.*, **37**, 1077–1093, https://doi.org/10.1002/rob.21947.

Gropp, M. E., and C. E. Davenport, 2018: The impact of the nocturnal transition on the lifetime and evolution of supercell thunderstorms in the Great Plains. *Wea. Forecasting*, **33**, 1045–1061, https://doi.org/10.1175/WAF-D-17-0150.1.

Hanft, W., and A. L. Houston, 2018: An observational and modeling study of mesoscale air masses with high theta-e. *Mon. Wea. Rev.*, **146**, 2503–2524, https://doi.org/10.1175/MWR-D-17-0389.1.

Hastings, R., and Y. Richardson, 2016: Long-term morphological changes in simulated supercells following mergers with nascent supercells in directionally varying shear. *Mon. Wea. Rev.*, **144**, 471–499, https://doi.org/10.1175/MWR-D-15-0193.1.

Healey, D. J., and M. S. Van Den Broeke, 2023: Comparing polarimetric signatures of proximate pretornadic and nontornadic supercells in similar environments. *Wea. Forecasting*, **38**, 2011–2027, https://doi.org/10.1175/WAF-D-23-0013.1.

Helmus, J. J., and S. M. Collis, 2016: The Python ARM radar toolkit (Py-ART), a library for working with weather radar data in the Python programming language. *J. Open Res. Software*, **4**, 25, https://doi.org/10.5334/jors.119.

Honda, T., and T. Kawano, 2016: A possible mechanism of tornadogenesis associated with the interaction between a supercell and an outflow boundary without horizontal shear. *J. Atmos. Sci.*, **73**, 1273–1292, https://doi.org/10.1175/JAS-D-14-0347.1.

Houston, A. L., B. Argrow, M. C. Coniglio, E. W. Frew, E. N. Rasmussen, C. C. Weiss, and C. L. Ziegler, 2020: Targeted observation by radars and UAS of supercells (TORUS): Summary of the 2019 field campaign. *Field Observations of Physical Processes to Understand Severe Storms*, Boston, MA, Amer. Meteor. Soc., 1.3, https://ams.confex.com/ams/2020Annual/meetingapp.cgi/Paper/369999.

Houston, A., K. Axon, and A. Erwin, 2021: UNL Combined Mesonet and Tracker (CoMeT-1) Mobile Mesonet Data, version

2.1. UCAR/NCAR–Earth Observing Laboratory, accessed 20 September 2022, https://doi.org/10.26023/B967-JN6J-AY03.

Jorgensen, D. P., C. L. Ziegler, E. N. Rasmussen, A. S. Goldstein, and A. A. Alford, 2017: Improvements to the NOAA P-3 airborne Doppler tail-mounted radar: Supercell observations from VORTEX-Southeast. *38th Conf. on Radar Meteorology*, Chicago, IL, Amer. Meteor. Soc., 6A.2, https://ams.confex.com/ams/38RADAR/webprogram/Paper320666.html.

Kessinger, C. J., P. S. Ray, and C. E. Hane, 1987: The Oklahoma squall line of 19 May 1977. Part I: A multiple Doppler analysis of convective and stratiform structure. *J. Atmos. Sci.*, **44**, 2840–2865, https://doi.org/10.1175/1520-0469(1987)044<2840:TOSLOM>2.0.CO;2.

King, J. R., M. D. Parker, K. D. Sherburn, and G. M. Lackmann, 2017: Rapid evolution of cool season, low-CAPE severe thunderstorm environments. *Wea. Forecasting*, **32**, 763–779, https://doi.org/10.1175/WAF-D-16-0141.1.

Klees, A. M., Y. P. Richardson, P. M. Markowski, C. Weiss, J. M. Wurman, and K. Kosiba, 2016: Comparison of the tornadic and nontornadic supercells intercepted by VORTEX2 on 10 June 2010. *Mon. Wea. Rev.*, **144**, 3201–3231, https://doi.org/10.1175/MWR-D-15-0345.1.

Koch, S. E., M. desJardins, and P. J. Kocin, 1983: An interactive Barnes objective map analysis scheme for use with satellite and conventional data. *J. Climate Appl. Meteor.*, **22**, 1487–1503, https://doi.org/10.1175/1520-0450(1983)022<1487:AIBOMA>2.0.CO;2.

——, R. Ware, H. Jiang, and Y. Xie, 2016: Rapid mesoscale environmental changes accompanying genesis of an unusual tornado. *Wea. Forecasting*, **31**, 763–786, https://doi.org/10.1175/WAF-D-15-0105.1.

Laflin, J. M., and A. L. Houston, 2012: A modeling study of supercell development in the presence of a preexisting airmass boundary. *Electron. J. Severe Storms Meteor.*, **7** (1), https://ejssm.com/ojs/index.php/site/issue/view/34.

Lee, B. D., B. F. Jewett, and R. B. Wilhelmson, 2006: The 19 April 1996 Illinois tornado outbreak. Part II: Cell mergers and associated tornado incidence. *Wea. Forecasting*, **21**, 449–464, https://doi.org/10.1175/WAF943.1.

——, C. A. Finley, and C. D. Karstens, 2012: The Bowdle, South Dakota, cyclic tornadic supercell of 22 May 2010: Surface analysis of rear-flank downdraft evolution and multiple internal surges. *Mon. Wea. Rev.*, **140**, 3419–3441, https://doi.org/10.1175/MWR-D-11-00351.1.

Maddox, R. A., 1993: Diurnal low-level wind oscillation and storm-relative helicity. *The Tornado: Its Structure, Dynamics, Prediction, and Hazards*, *Geophys. Monogr.*, Vol. 79, Amer. Geophys. Union, 591–598, https://doi.org/10.1029/GM079p0591.

——, L. R. Hoxit, and C. F. Chappell, 1980: A study of tornadic thunderstorm interactions with thermal boundaries. *Mon. Wea. Rev.*, **108**, 322–336, https://doi.org/10.1175/1520-0493(1980)108<0322:ASOTTI>2.0.CO;2.

Magee, K. M., and C. E. Davenport, 2020: An observational analysis quantifying the distance of supercell-boundary interactions in the Great Plains. *J. Oper. Meteor.*, **8**, 15–38, https://doi.org/10.15191/nwajom.2020.0802.

Majcen, M., P. Markowski, Y. Richardson, D. Dowell, and J. Wurman, 2008: Multipass objective analyses of Doppler radar data. *J. Atmos. Oceanic Technol.*, **25**, 1845–1858, https://doi.org/10.1175/2008JTECHA1089.1.

Markowski, P. M., 2020: What is the intrinsic predictability of tornadic supercell thunderstorms? *Mon. Wea. Rev.*, **148**, 3157–3180, https://doi.org/10.1175/MWR-D-20-0076.1.

——, and Y. P. Richardson, 2014: The influence of environmental low-level shear and cold pools on tornadogenesis: Insights from idealized simulations. *J. Atmos. Sci.*, **71**, 243–275, https://doi.org/10.1175/JAS-D-13-0159.1.

——, E. N. Rasmussen, and J. M. Straka, 1998: The occurrence of tornadoes in supercells interacting with boundaries during VORTEX-95. *Wea. Forecasting*, **13**, 852–859, https://doi.org/10.1175/1520-0434(1998)013<0852:TOOTIS>2.0.CO;2.

——, and Coauthors, 2012: The pretornadic phase of the Goshen County, Wyoming, supercell of 5 June 2009 intercepted by VORTEX2. Part II: Intensification of low-level rotation. *Mon. Wea. Rev.*, **140**, 2916–2938, https://doi.org/10.1175/MWR-D-11-00337.1.

May, R. M., and Coauthors, 2022: MetPy: A meteorological Python library for data analysis and visualization. *Bull. Amer. Meteor. Soc.*, **103**, E2273–E2284, https://doi.org/10.1175/BAMS-D-21-0125.1.

Mead, C. M., and R. L. Thompson, 2011: Environmental characteristics associated with nocturnal significant-tornado events in the central and southern Great Plains. *Electron. J. Severe Storms Meteor.*, **6** (6), https://doi.org/10.55599/ejssm.v6i6.33.

Naylor, J., and M. S. Gilmore, 2012: Convective initiation in an idealized cloud model using an updraft nudging technique. *Mon. Wea. Rev.*, **140**, 3699–3705, https://doi.org/10.1175/MWR-D-12-00163.1.

Nelson, S. P., and R. A. Brown, 1982: Multiple Doppler radar derived vertical velocities in thunderstorms. Part I: Error analysis and solution techniques; Part II: Maximizing areal extent of vertical velocities. NOAA Tech. Memo. ERL NSSL-94, 29 pp., https://repository.library.noaa.gov/view/noaa/17603.

O'Brien, J. J., 1970: Alternative solutions to the classical vertical velocity problem. *J. Appl. Meteor.*, **9**, 197–203, https://doi.org/10.1175/1520-0450(1970)009<0197:ASTTCV>2.0.CO;2.

Peters, J. M., C. J. Nowotarski, and G. L. Mullendore, 2020: Are supercells resistant to entrainment because of their rotation? *J. Atmos. Sci.*, **77**, 1475–1495, https://doi.org/10.1175/JAS-D-19-0316.1.

Rasmussen, E. N., and D. O. Blanchard, 1998: A baseline climatology of sounding-derived supercell and tornado forecast parameters. *Wea. Forecasting*, **13**, 1148–1164, https://doi.org/10.1175/1520-0434(1998)013<1148:ABCOSD>2.0.CO;2.

——, S. Richardson, J. M. Straka, P. M. Markowski, and D. O. Blanchard, 2000: The association of significant tornadoes with a baroclinic boundary on 2 June 1995. *Mon. Wea. Rev.*, **128**, 174–191, https://doi.org/10.1175/1520-0493(2000)128<0174:TAOSTW>2.0.CO;2.

Ray, P. S., and K. L. Sangren, 1983: Multiple-Doppler radar network design. *J. Climate Appl. Meteor.*, **22**, 1444–1454, https://doi.org/10.1175/1520-0450(1983)022<1444:MDRND>2.0.CO;2.

——, K. K. Wagner, K. W. Johnson, J. J. Stephens, W. C. Bumgarner, and E. A. Mueller, 1978: Triple-Doppler observations of a convective storm. *J. Appl. Meteor.*, **17**, 1201–1212, https://doi.org/10.1175/1520-0450(1978)017<1201:TDOOAC>2.0.CO;2.

——, C. L. Ziegler, W. Bumgarner, and R. J. Serafin, 1980: Single- and multiple-Doppler radar observations of tornadic storms. *Mon. Wea. Rev.*, **108**, 1607–1625, https://doi.org/10.1175/1520-0493(1980)108<1607:SAMDRO>2.0.CO;2.

Raymond, W., 1988: High-order low-pass implicit tangent filters for use in finite area calculations. *Mon. Wea. Rev.*, **116**, 2132–2141, https://doi.org/10.1175/1520-0493(1988)116<2132:HOLPIT>2.0.CO;2.

Rogers, J., 2012: Significant tornado events associated with cell mergers. *26th Conf. on Severe Local Storms*, Nashville, TN,

Amer. Meteor. Soc., 9.4, https://ams.confex.com/ams/26SLS/webprogram/Paper211575.html.

——, and C. Weiss, 2008: The association of cell mergers with tornado occurrence. *24th Conf. on Severe Local Storms*, Savannah, GA, Amer. Meteor. Soc., P3.23, https://ams.confex.com/ams/pdfpapers/141784.pdf.

Skinner, P. S., C. C. Weiss, M. M. French, H. B. Bluestein, P. M. Markowski, and Y. P. Richardson, 2014: VORTEX2 observations of a low-level mesocyclone with multiple internal rear-flank downdraft momentum surges in the 18 May 2010 Dumas, Texas, supercell. *Mon. Wea. Rev.*, **142**, 2935–2960, https://doi.org/10.1175/MWR-D-13-00240.1.

Smith, B. T., R. L. Thompson, J. S. Grams, C. Broyles, and H. E. Brooks, 2012: Convective modes for significant severe thunderstorms in the contiguous United States. Part I: Storm classification and climatology. *Wea. Forecasting*, **27**, 1114–1135, https://doi.org/10.1175/WAF-D-11-00115.1.

Thompson, R. L., R. Edwards, J. A. Hart, K. L. Elmore, and P. Markowski, 2003: Close proximity soundings within supercell environments obtained from the Rapid Update Cycle. *Wea. Forecasting*, **18**, 1243–1261, https://doi.org/10.1175/1520-0434(2003)018<1243:CPSWSE>2.0.CO;2.

Wakimoto, R. M., C. Liu, and H. Cai, 1998: The Garden City, Kansas, storm during VORTEX 95. Part I: Overview of the storm life cycle and mesocyclogenesis. *Mon. Wea. Rev.*, **126**, 372–392, https://doi.org/10.1175/1520-0493(1998)126<0372:TGCKSD>2.0.CO;2.

Waugh, S., 2020a: NSSL Mobile Quality Controlled (QC) Radiosonde Data, version 1.0. UCAR/NCAR–Earth Observing Laboratory, accessed 1 September 2022, https://doi.org/10.26023/MDEM-SG4J-5P10.

——, 2020b: NSSL Mobile Mesonet Data, version 1.1. UCAR/NCAR–Earth Observing Laboratory, accessed 21 September 2022, https://doi.org/10.26023/2Y87-XEEB-7W13.

——, 2021: The "U-Tube": An improved aspirated temperature system for mobile meteorological observations, especially in severe weather. *J. Atmos. Oceanic Technol.*, **38**, 1477–1489, https://doi.org/10.1175/JTECH-D-21-0008.1.

Wurman, J., Y. Richardson, C. Alexander, S. Weygandt, and P. F. Zhang, 2007: Dual-Doppler and single-Doppler analysis of a tornadic storm undergoing mergers and repeated tornadogenesis. *Mon. Wea. Rev.*, **135**, 736–758, https://doi.org/10.1175/MWR3276.1.

Ziegler, C. L., 2013: A diabatic Lagrangian technique for the analysis of convective storms. Part II: Application to a radar-observed storm. *J. Atmos. Oceanic Technol.*, **30**, 2266–2280, https://doi.org/10.1175/JTECH-D-13-00036.1.

——, 2020: NOAA P-3 Tail Mounted X-Band Doppler Radar, version 1.0. UCAR/NCAR–Earth Observing Laboratory, accessed 16 February 2021, https://doi.org/10.26023/R2AS-DBCT-S0P.

——, E. R. Mansell, J. M. Straka, D. R. MacGorman, and D. W. Burgess, 2010: The impact of spatial variations of low-level stability on the life cycle of a simulated supercell storm. *Mon. Wea. Rev.*, **138**, 1738–1766, https://doi.org/10.1175/2009MWR3010.1.

——, T. A. Murphy, K. L. Elmore, M. I. Biggerstaff, Z. Wang, E. N. Rasmussen, D. P. Jorgensen, and A. A. Alford, 2018: Kinematics, thermodynamics, and microphysics of the tornadic 13–14 April 2018 Calhoun, LA supercell during VORTEX-SE. *29th Conf. on Severe Local Storms*, Stowe, VT, Amer. Meteor. Soc., 8.4, https://ams.confex.com/ams/29SLS/webprogram/Paper348224.html.